Consortium

for

Small–Scale Modelling

Technical Report No. 7

Lorenz- and Charney-Phillips vertical grid experimentation using a compressible nonhydrostatic toy-model relevant to the fast-mode part of the 'Lokal - Modell'

by

H.-J. Herzog and A. Gassmann

Res severa verum gaudium !

February 2005

DOI: 10.5676/DWD_pub/nwv/cosmo-tr_7

Deutscher Wetterdienst

MeteoSwiss

Ufficio Generale per la Meteorologia

Hellenic National Meteorological Service

Instytut Meteorologii i Gospodarki Wodnej

Il Servicio Meteorologico Regionale di ARPA

Amt für Wehrgeophysik

L'Agenzia Regionale per la Protenzione Ambientale del Piemonte

www.cosmo-model.org

Editors: G. Doms and U. Schättler, Deutscher Wetterdienst, P.O. Box 100465, 63004 Offenbach, Germany
Printed at Deutscher Wetterdienst, Offenbach am Main

Contents

1 Introduction

It is well known that in numerical atmospheric simulation models for vertical discretisation a so-called Lorenz (L-)-grid or a Charney-Phillips (CP-)-grid is normally applied in order to define the staggered placement of model variables at grid points along the vertical. In case of an L-grid the variables of temperature, pressure and horizontal momentum are placed at 'main-levels', each of them centred within a finite model layer, while the vertical velocity is assumed to be positioned at 'half-levels', which are the interface levels between adjacent model layers. The difference of the CP-grid to the L-grid consists in having placed temperature together with vertical velocity at half-levels. For instance, the Lokal-Modell of the DWD uses an L-grid, while the Unified Model of the United Kingdom Met Office is based on a CP-grid. A representative discussion of pros and cons concerning both types of vertical grid staggering can be found in a thorough paper by Arakawa (2000). There, Arakawa gives statements and draws conclusions from his own work and so from many other authors that the CP-grid seems preferable compared to the L-grid also widespread in use. In order to characterise an obvious shortcoming of the L-grid we quote from Arakawa's article (2000, p.721-780) the following statement: 'The problem with the L-grid is due to the existence of an extra degree of freedom in the vertical distribution of θ that cannot be controlled by any baroclinic (or internal) modes... This extra degree of freedom introduces a vertical "computational mode" in the solution, characterised by a zigzag vertical structure of θ, which has no counterpart in the solutions of the continuous equation... It is important to note, that this problem with the L Grid is a property of the grid rather than of a particular scheme. An increase in order of accuracy does not reduce the error due to this mode because a computational mode cannot become "accurate" since there is no corresponding true solution with which to compare it.'
This statement is a more general motivation, but due to the fact that the Lokal-Modell (=LM) as a model of particular interest uses an L-grid, our concern and starting point comes immediately from a paper by Arakawa and Konor (1996). In this article the main point we are interested in is the author's comparing numerical simulations with the L-grid and the CP-grid. For this, they use two linearised versions of a primitive equation model for meridionally uniform perturbations, one for the grid type L and the other for the CP-grid. In order to show the existence of a computational mode produced by the L-grid and to demonstrate that this artificial effect is avoided in case of a CP-grid, a local initial potential temperature perturbation as one specific set of integration is imposed on a resting isothermal ($T_0 = 250K$) basic state on a zonally cyclic f-plane. The model uses simple centered vertical differences on a p-coordinate and 40 equally spaced layers below 100 Pa. For a detailed description of the model equations and the experimental set-up we refer to Arakawa and Konor (1996). The unbalanced initial perturbation in $\theta^{'}$ is set equal to 0.5 K at levels with vertical index k=39/39.5 (k-index is counted downward), and with opposite sign at the adjacent level designed by k=38/38.5 for the L-grid/CP-grid, and $\theta^{'} = 0$ everywhere else.
As an introduction for our own numerical experimentation we deliberately describe and show the experimental set-up and important results from Arakawa and Konor, concerning the isolated effect of a computational mode due to the L-grid. In Figure 1 an important result from the author's original paper is therefore shown again (original Figure 3 from Monthly Weather Review 124, at page 521): The original legend is sufficiently self-explaining. It shows in a time-height plot the evolution over 48 hours integration time of an initially specified spectral perturbation amplitude for two horizontal wave components with a wavelength of 100 km and 250 km, respectively. From another quotation in the relevant paper that simulation result may be characterised as follows. In case of the L-grid simulation '... The flow is dominated by stationary components... The vertically propagating oscillatory component is weak, having significant amplitudes only during early hours.' A pure artificial vertical zigzag structure is obvious. For the CP-grid, however, '... The simulation shows vertical propagation and almost complete dispersion of initial perturbations...' and a stationary computational mode does not occur.

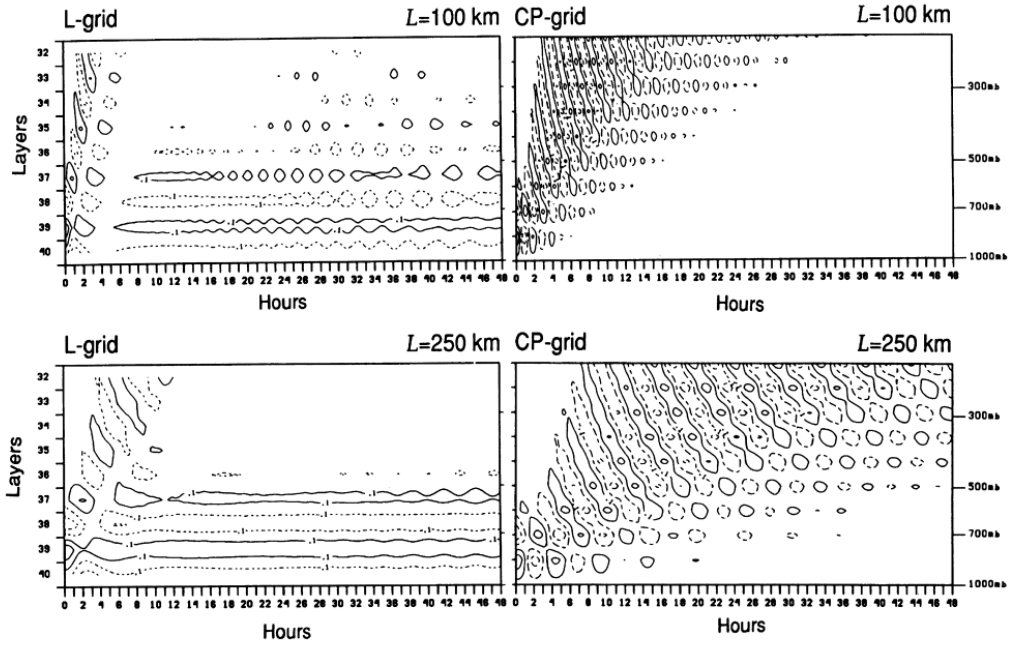

FIG. 3. Time evolution of the potential temperature perturbation θ' (K) in the lower portion of the vertical domain obtained from the models based on the Lorenz (left panels) and Charney–Phillips (right panels) grids for horizontal wavelengths L = 100 km (upper panels) and L = 250 km (lower panels). Simulations are started from unbalanced θ' at two adjacent levels with opposite signs. Solid and dashed lines correspond to positive and negative values, respectively. The contour interval is 0.2 K starting from ±0.1 K.

Figure 1: Original figure taken from Arakawa, A., and C.S. Konor, 1996 (see References)

In a first step of our following numerical simulations we are going to copy as exact as possible both the hydrostatic simulation model and the numerical set-up from Arakawa and Konor's paper, who provide the reader with a fairly good description of their approach. On this ground we were then easily able to copy the results from and could have obtained in such a way a comfortable method, and also an appropriate calibration tool, for our concern with a nonhydrostatic model having important characteristics of the fast-mode part of the LM. With the adopted thickness and number of model layers we were able to demonstrate for the LM-like compressible nonhydrostatic model with L-grid versus CP-grid simulation results similar to Arakawa and Konor's in case of hydrostatic gravity waves, where a computational mode is revealed in case of the L-grid type model, while it is avoided by using a CP-type model. To obtain this sort of simulations in a fairly neat form, we felt it necessary to introduce, in addition, a non-reflective upper boundary condition. Instead of a Rayleigh relaxation-type we have applied an radiative upper boundary condition (=RUBC) as suggested from Klemp and Durran (1983) and Bougeault (1983). Within the scope of this LM-toy model with essential components of the fast mode part of the real LM the possible occurrence of a computational mode due to the L-grid and the application of a CP-grid instead in order to avoid this numerical nuisance will be demonstrated. At this stage of work it seems however too early for a generalisation of that simulation results to draw already the conclusion that the vertical grid staggering in the LM should be changed from the L- to the CP-grid immediately. Neverthless, the results demonstrated in this contribution give serious hints that the LM is suspected to have possible unwanted numerical shortcomings related to the applied L-grid which are worth studying further in a more specific and systematic manner. The importance of this should be underlined by still another quotation from the key paper of Arakawa and Konor: 'The problem of the existence of the computational mode can be serious, especially in the models that include moist processes, since the computational mode can spuriously interact with the physical mode through inherently nonlinear condensation and associated processes. An example of the latter is the effect of cloud layers generated by the zigzag vertical structure of the potential temperature on the radiation field.'

2 A duplicate of Arakawa and Konor's simulation

As explained above we are interested in an almost exact repetition of numerical simulations from Arakawa and Konor (1996). Their results have been depicted in our Figure 1 (taken from the original paper). With strict quotation from that paper all the background may be assumed to be known, that is, how this simulation experiment has been conducted and the model and the numerics were

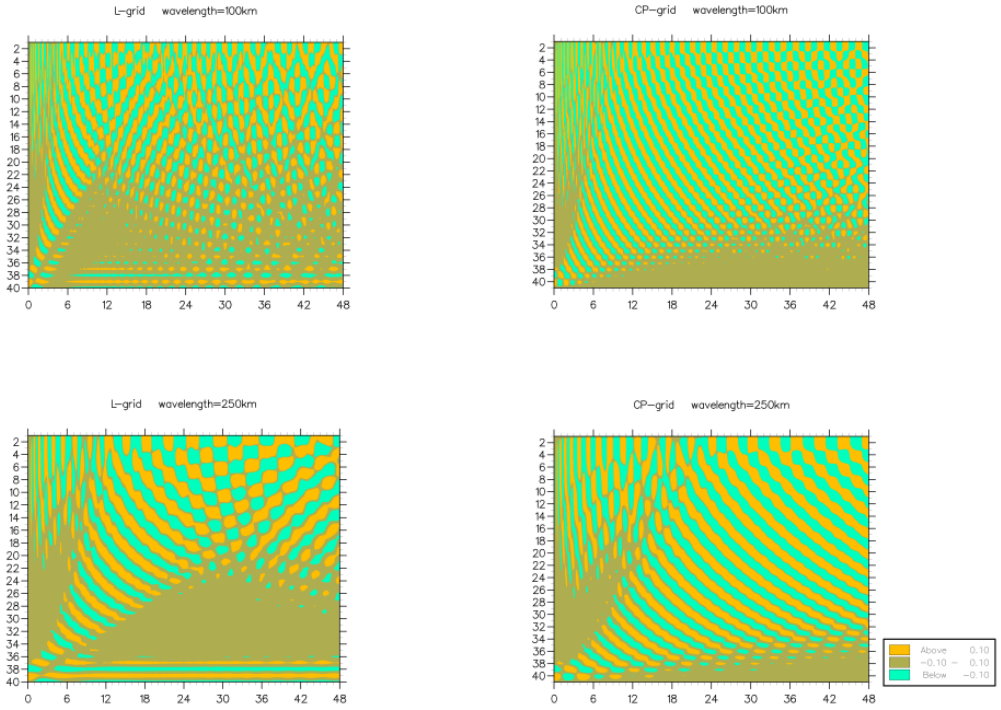

Figure 2: Almost the same result as in Figure 1, but over the entire integration domain, for L-grid (left panels) and CP-grid (right panels) and for horizontal wavelengths 100km (upper panels) and 250km (lower panels). For more details see text.

designed. Moreover, the comments describing the special experiment were already noted in the Introduction and need not be repeated here. In order to almost copy the result of interest shown in Figure 1, we decided to apply the leap-frog scheme as an sufficient numerical time-integration method, and for sake of caution, an Asselin time filter is added at every time step. In case of the model version with L=250km, the time step is chosen $\Delta t = 90s$, for L=100km we used $\Delta t = 30s$. In this way we are now in a position to be able to show the almost identical outcome, but here over the entire integration area, from the lower boundary (at 100000 Pa) up to the upper boundary (at 100 Pa) over 40 equally spaced layers, where the time evolution of the potential temperature perturbation in the lowest 9 layers of Figure 1 is recovered fairly good in Figure 2. In addition to a qualitative discussion of Figure 1 , and so of Figure 2, we make out that the gravity wave perturbations, here expressed in terms of potential temperature and caused by the defined initial state, propagate upward over a wider range of signal velocities different in dependence of an L-grid or a CP-grid, and that in any case these propagating perturbations are reflected at the upper boundary due to an lid condition imposed there. The reflected wave component as an obvious artificial phenomenon can then 'contaminate' in case of the L-grid even the computational mode of our concern. For the smaller spectral component with L=100km the degree of reflection seems more obvious than for L=250km, and for the experimental set with an CP-grid the strength of reflection seems apparently reduced compared to the model version with L-grid.

In the following we are interested in eliminating the reflected wave mode, which may be done by use of a radiative upper boundary condition (RUBC) instead of the lid condition. For the Arakawa-Konor model (AKM), which is linear and a hydrostatic one, the Klemp-Durran-Bougeault typ of an RUBC (=KDB-RUBC) is expected to be sufficient as an appropriate tool. Since the model variables in the AKM are spectral amplitudes of a horizontal wave component depending on pressure and time, the application of the KDB-RUBC is ideal. As known, this BC is local in time but global over the upper boundary level. In general, this needs the Fourier transforms of vertical motion and a mass variable at the upper boundary. Here, the RUBC is easily formulated in terms of the defined model variables without an additional transform. The reader may be convinced about this from a necessary reference to the original paper of Arakawa and Konor (1996). After a thorough and classical analysis we can derive the appropriate RUBC for the given AKM. It reads

$$\hat{\omega}_{top} = -\frac{k\ p_{top}}{c_0}\hat{\phi}_{top} \tag{1}$$

instead of the lid condition $\hat{\omega}_{top} = 0$. For the perturbation geopotential and vertical velocity variables of the given model we have

$$\phi^{'}(x,p,t) = \hat{\phi}(p,t)\ sin\, kx \quad , \quad \omega^{'}(x,p,t) = \hat{\omega}(p,t)\ sin\, kx \tag{2}$$

with horizontal wavenumber $k = 2\pi/L$, $p_{top} = 100\,Pa$, and the parameter $c_0 = +\sqrt{\kappa R T_0}, \kappa = c_p/c_v$. Here we make use of the normal meteorological notation also valid for the AKM . This form of a KDB-RUBC has been applied in the AKM for both its L-grid and its CP-grid version. It is important to note that in accordance with (1) the geopotential needed at the upper boundary (the uppermost half-level) must be extrapolated by use of an uncentered difference form of the hydrostatic equation different for L-grid and CP-grid due to different positions of the potential temperature on these grids. In that way we have repeated the AKM simulations, and the corresponding results are shown in Figure 3 [1] for the case with L =100km.

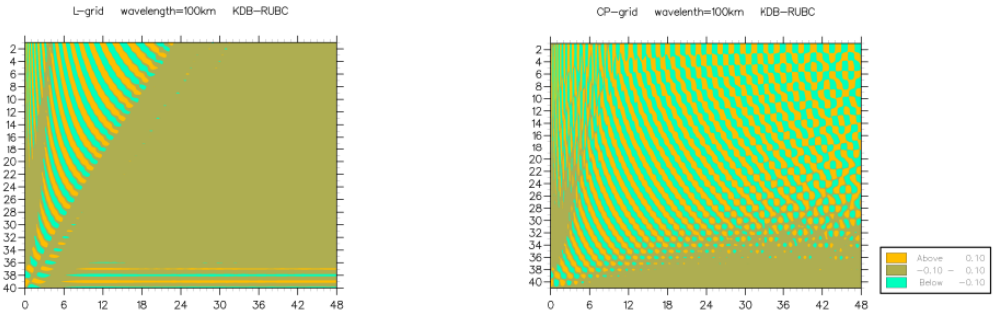

Figure 3: Repetition of Arakawa and Konor's (1996) simulation for L-grid and CP- grid with L =100km, but a radiative upper boundary condition taken into account (compare with upper panel of Figure 2).

A comparison with Figure 2 demonstrates that the reflection from the upper boundary could be removed as desired. Similar results not shown here were found for the wavelength L= 250km. In contrast to the CP-grid, we observe for the L-grid simulation a significant limitation of the gravity wave dispersion process accompanied by the stationary zigzag phenomenon of a computational mode.

[1] It needs a technical remark concerning Figures 2 and 3 and so on all Figures of this type. The contour colours are meant as follows: *brown* covers an interval from $\pm 0.1\ K$, *yellow* covers values $> 0.1\ K$, and *green* is valid for $< -0.1\ K$

3 An LM fast-wave toy-model

With the information from Arakawa and Konor's simulation example, we turn now to the compressible nonhydrostatic equations in a linearised form, having in mind the relation to the fast-mode part of the LM. For this we refer to a thorough description of the LM dynamics and numerics documented by Doms and Schättler (2002). On this ground we are going to derive an appropriate simulation model with properties as much as possible of Arakawa and Konor's model set-up.

3.1 Model equation set

Starting point is the following equation set

$$\frac{\partial u'}{\partial t} = -\frac{1}{\bar{\rho}}\left(\frac{\partial p'}{\partial x} - \frac{1}{\sqrt{\gamma}}\frac{\partial \bar{p}}{\partial x}\frac{\partial p'}{\partial \zeta}\right) + f_0 v' \tag{3}$$

$$\frac{\partial v'}{\partial t} = \quad -f_0 v' \tag{4}$$

$$\frac{\partial w'}{\partial t} = \frac{g}{\sqrt{\gamma}}\frac{\partial p'}{\partial \zeta} - g\left(\frac{p'}{\bar{p}} - \frac{T'}{\bar{T}}\right) \tag{5}$$

$$\frac{\partial p'}{\partial t} = g\bar{\rho}w' - \kappa\bar{p}\left(\frac{\partial u'}{\partial x} - \frac{1}{\sqrt{\gamma}}\frac{\partial \bar{p}}{\partial x}\frac{\partial u'}{\partial \zeta} - \frac{g\bar{\rho}}{\sqrt{\gamma}}\frac{\partial w'}{\partial \zeta}\right) \tag{6}$$

$$\frac{\partial T'}{\partial t} = \frac{g\bar{\rho}}{\sqrt{\gamma}}\frac{d\bar{T}}{d\zeta}w' - \frac{\kappa}{c_p}\frac{\bar{p}}{\bar{\rho}}\left(\frac{\partial u'}{\partial x} - \frac{1}{\sqrt{\gamma}}\frac{\partial \bar{p}}{\partial x}\frac{\partial u'}{\partial \zeta} - \frac{g\bar{\rho}}{\sqrt{\gamma}}\frac{\partial w'}{\partial \zeta}\right) \tag{7}$$

These equations follow approximately from the fast-mode equation part of the LM by consequent linearisation. The perturbation variables (primed entities) are assumed to be meridionally uniform. Spherical metric terms have been dropped for the sake of simplicity. The variables $\bar{p}$, $\bar{\rho}$, $\bar{T}$ constitute a hydrostatic basic state. The vertical coordinate ζ is meant just as in the LM. In relation to the usual z-coordinate the following operator is valid

$$\frac{\partial}{\partial z} = -\frac{g\bar{\rho}}{\sqrt{\gamma}}\frac{\partial}{\partial \zeta} \tag{8}$$

Here, the reciprocal pre-factor $\left(\sqrt{\gamma}\right) / \left(g\bar{\rho}\right)$ is defined as the Jacobian of the transformation from the z- to the ζ - coordinate. The equation set (3) - (7) deviates slightly from the present formulation in the fast-wave part of the LM. In order to take into account inertia-gravity waves, that is without separation of the rotational effect, the Coriolis terms are included here. Further, we emphasize the presence of the first term on the right-hand side of equation (7), which is significant in case of a non-isothermal basic state as it is for the LM. There, a polytropic state is stipulated. Neglecting the term in that case leads however to an inconsistency concerning the gravity wave energetics and an overestimation of the gravity wave frequencies. To evade this problem a-priori, a prognostic equation for θ' should be used rather than for T'. We do so , although from the discussed point of view unnecessary, because we prefer an isothermal basic state which makes that term vanishing.

With this choice we are deliberately in accordance with the basic state of the AKM. Without any loss of physical background the vertical z- coordinate is simply taken, and a horizontally plane terrain may be sufficient for our considerations to be assumed. Thus, we change with these assumptions from (3) - (7) to a physically identical set

$$\frac{\partial u^{'}}{\partial t} = -\frac{1}{\bar{\rho}}\frac{\partial p^{'}}{\partial x} + f_0 v \tag{9}$$

$$\frac{\partial v^{'}}{\partial t} = -f_0 u^{'} \tag{10}$$

$$\frac{\partial w^{'}}{\partial t} = -\frac{1}{\bar{\rho}}\frac{\partial p^{'}}{\partial z} - \frac{g}{\bar{\rho}\, c_s^2}\, p^{'} + \frac{g}{\bar{\theta}}\theta^{'} \tag{11}$$

$$\frac{\partial p^{'}}{\partial t} = g\bar{\rho} w^{'} - c_s^2 \bar{\rho}\left(\frac{\partial u^{'}}{\partial x} + \frac{\partial w^{'}}{\partial z}\right) \tag{12}$$

$$\frac{\partial \theta^{'}}{\partial t} = -\frac{N^2}{g}\bar{\theta}\; w^{'} \tag{13}$$

For the isothermal basic state we have

$$N^2 = \frac{g}{\bar{\theta}}\frac{d\bar{\theta}}{d\, z} = \frac{g^2}{c_p\, T_0}\;\;,\;\; \bar{\theta} = T_0\; exp\left(\frac{N^2}{g} z\right)\;\;,\;\; \bar{\rho} = \frac{p_s}{R\, T_0}\; exp\left(-\frac{g}{c_p T_0} z\right) \tag{14}$$

with the familiar constants $c_s^2 = \kappa\bar{p}/\bar{\rho} = \kappa\; RT_0\;\;,\;\; \kappa = c_p/c_v\;\;,\;\; T_0 = 250K$, and $p_s = 100000\, Pa$ at the lower boundary. In order to perform similar numerical experiments as Arakawa and Konor (1996) demonstrated, we assume also that the perturbations are horizontally standing waves in the forms:

$$\begin{gathered} u^{'}(x,z,t) = \hat{u}(z,t)\, cos\, kx\;\;,\;\; v^{'}(x,z,t) = \hat{v}(z,t)\, cos\, kx \\ w^{'}(x,z,t) = \hat{w}(z,t)\, sin\, kx\;\;,\;\; p^{'}(x,z,t) = \hat{p}(z,t)\, sin\, kx\;\;,\;\; \theta^{'}(x,z,t) = \hat{\theta}(z,t)\, sin\, kx \end{gathered} \tag{15}$$

$k = 2\pi/L$ is the zonal wavenumber with the wavelength L . Inserting the wave-components (15) into the above equation set, we obtain a simple prognostic equation system for the perturbation amplitudes of their horizontal wave-components with wavelength L :

$$\frac{\partial \hat{u}}{\partial t} = -\frac{k}{\bar{\rho}}\hat{p} + f_0 \hat{v} \tag{16}$$

$$\frac{\partial \hat{v}}{\partial t} = -f_0 \hat{u} \tag{17}$$

$$\frac{\partial \hat{w}}{\partial t} = -\frac{1}{\bar{\rho}}\frac{\partial \hat{p}}{\partial z} - \frac{g}{\hat{\rho} c_s^2}\hat{p} + \frac{g}{\bar{\theta}}\hat{\theta} \tag{18}$$

$$\frac{\partial \hat{p}}{\partial t} = g\bar{\rho}\hat{w} - c_s^2\bar{\rho}\left(\frac{\partial \hat{w}}{\partial z} - k\,\hat{u}\right) \tag{19}$$

$$\frac{\partial \hat{\theta}}{\partial t} = -\frac{N^2\bar{\theta}}{g}\hat{w} \tag{20}$$

The associated local total energy budget equation reads

$$\frac{\partial}{\partial t}\left[\frac{1}{2}\bar{\rho}\left(\hat{u}^2+\hat{v}^2+\hat{w}^2\right) + \frac{1}{2c_s^2\bar{\rho}}\hat{\rho}^2 + \frac{g^2\bar{\rho}}{2N^2}\left(\frac{\hat{\theta}}{\bar{\theta}}\right)^2\right] = -\frac{\partial\left(\hat{p}\;\hat{w}\right)}{\partial z} \tag{21}$$

and, for some reasoning further below, we note here the normal mode frequencies for the internal gravity waves solution (ω_g) and the acoustic wave solution (ω_a) of the equation set (16) - (20) with the rotational effect ignored $(f_0 = 0)$, following an usual analysis:

$$\omega_a^2 \approx c_s^2\left(k^2+n^2+\frac{1}{4H^2}\right) \tag{22}$$

$$\omega_g^2 \approx \frac{k^2N^2}{k^2+n^2+\frac{1}{4H^2}} \tag{23}$$

n denotes a vertical wavenumber, and H , $\left(H^{-1} = g/c_s^2 + N^2/g\right)$, a constant vertical scale height.

3.2 Time differencing scheme

For our linear system (16) - (20) we are going to adopt the time integration scheme as close as possible from the fast mode part of the LM. To compare that with the LM we refer to the thorough LM-documentation by Doms and Schättler (2002) and there with further quotations of Skamarock and Klemp (1992), Ikawa (1988), and Dudhia (1993). With that application we have here

$$\frac{\hat{u}^{(\tau+1)} - \hat{u}^{(\tau)}}{\Delta t} = -\frac{k}{\bar{\rho}}\hat{p}^{(\tau)} + f_0\hat{v}^{(\tau+1)} \tag{24}$$

$$\frac{\hat{v}^{(\tau+1)} - \hat{v}^{(\tau)}}{\Delta t} = -f_0\hat{u}^{(\tau+1)} \tag{25}$$

$$\begin{aligned}\frac{\hat{w}^{(\tau+1)} - \hat{w}^{(\tau)}}{\Delta t} = &-\frac{1}{\bar{\rho}}\left(\beta^+\frac{\partial \hat{p}^{(\tau+1)}}{\partial z} + \beta^-\frac{\partial \hat{p}^{(\tau)}}{\partial z}\right)\\ &-\frac{g}{\bar{\rho}c_s^2}\left(\beta^+\hat{p}^{(\tau+1)} + \beta^-\hat{p}^{(\tau)}\right) + \frac{g}{\bar{\theta}}\hat{\theta}^{(\tau)}\end{aligned} \tag{26}$$

$$\begin{aligned}\frac{\hat{p}^{(\tau+1)} - \hat{p}^{(\tau)}}{\Delta t} = &\;g\bar{\rho}\left(\beta^+\hat{w}^{(\tau+1)} + \beta^-\hat{w}^{(\tau)}\right)\\ &-c_s^2\bar{\rho}\left(\beta_+\frac{\partial \hat{w}^{(\tau+1)}}{\partial z} + \beta^-\frac{\partial \hat{w}^{(\tau)}}{\partial z}\right) + c_s^2\bar{\rho}\,k\,\hat{u}^{(\tau+1)}\end{aligned} \tag{27}$$

$$\frac{\hat{\theta}^{(\tau+1)} - \hat{\theta}^{(\tau)}}{\Delta t} = -\frac{N^2\bar{\theta}}{g}\left(\beta^+\hat{w}^{(\tau+1)} + \beta^-\hat{w}^{(\tau)}\right) \tag{28}$$

As one can see, the terms for vertically propagating waves are treated implicitly. For the weights of averaging these terms we have

$$\beta^+ = \frac{1}{2}(1+\varepsilon) \quad , \quad \beta^- = \frac{1}{2}(1-\varepsilon) \tag{29}$$

with the LM default-value $\varepsilon = 0.4$, determining the strength of implicity of the scheme. Since the scheme in this form behaves neutral for acoustic waves, a so-called divergence damping is added in the horizontal momentum equations as a remedy, which in our case means that in equation (24) the pressure in the gradient term is replaced such

$$\hat{p}^{(\tau)} := \hat{p}^{(\tau)} + \alpha_d\,\Delta t\,\bar{\rho}c_s^2\left(k\,\hat{u}^{(\tau)} - \frac{\partial\hat{w}^{(\tau)}}{\partial z}\right) \tag{30}$$

$\alpha_d = 0.1$ is the default-value used in the LM. We drop here critical remarks concerning this measure. The inclusion of the rotation terms in the momentum equations deviates from the LM fast-mode part, but is a concession to the AKM with which we want to compare our solutions. For the sake of stability these terms are formulated implicitly.

3.3 Vertical discretisation with an L-grid

In addition to the semi-discrete equations (24)- (28) with an LM-specific time differencing scheme, we want to exactly apply the vertical layering from the AKM with either an L-grid or a CP-grid. We introduce the L-grid first. In this way the scheme is shown in Figure 4

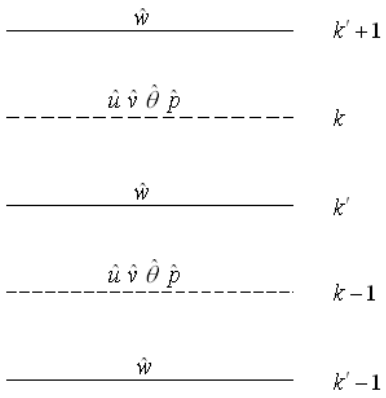

Figure 4: Vertical staggering of variables of LM fast-wave toy-model with equally spaced layers in accordance with AKM (see text)

As can be seen, the variables $\hat{u}, \hat{v}, \hat{\theta}, \hat{p}$ (and also $\bar{\rho}, \bar{\theta}$, not shown in Figure 4) are positioned at main-levels indicated with indices $k \in [1, ke]$, while the perturbation amplitude of vertical velocity, $\hat{w}$, is defined at so-called half-levels with index numbering $k^{'} \in [1, ke1]$. Coinciding with the numerical set-up in the AKM, we assume 40 model layers, which means $ke = 40$ and $ke1 = ke + 1$. In accordance with a vertical z-coordinate the index k is counted upward here, which is in contrast to

the LM with its terrain-following coordinate. The thickness of model-layers is constant. It is given by

$$\Delta z = \frac{1}{40}\frac{RT_0}{g} ln(1000) \qquad . \tag{31}$$

With that scheme we introduce simple centred differences in the vertical in the equation system (24) - (28), which leads straightforward to the following difference equation system:

$$\hat{u}_k^{(\tau+1)} = \hat{u}_k^{(\tau)} - \Delta t \frac{k}{\bar{\rho}} \hat{p}_k^{(\tau)} + f_0 \, \Delta t \, \hat{v}_k^{(\tau+1)} \tag{32}$$

$$\hat{v}_k^{(\tau+1)} = \hat{v}_k^{(\tau)} - \Delta t \, f_0 \, \hat{u}_k^{(\tau+1)} \tag{33}$$

for $k \in [1, ke]$.

$$\begin{aligned} \hat{w}_{k'}^{(\tau+1)} = \hat{w}_{k'}^{(\tau)} &- \frac{2}{\bar{\rho}_{k-1} + \bar{\rho}_k} \left(\frac{\Delta t}{\Delta z}\right) \beta^+ \left(\hat{p}_k^{(\tau+1)} - \hat{p}_{k-1}^{(\tau+1)}\right) \\ &- \frac{2}{\bar{\rho}_{k-1} + \bar{\rho}_k} \left(\frac{g\Delta t}{2c_s^2}\right) \beta^+ \left(\hat{p}_k^{(\tau+1)} + \hat{p}_{k-1}^{(\tau+1)}\right) + C_{k'}^w \end{aligned} \tag{34}$$

with

$$\begin{aligned} C_{k'}^w = &- \frac{2}{\bar{\rho}_{k-1} + \bar{\rho}_k} \left(\frac{\Delta t}{\Delta z}\right) \beta^- \left(\hat{p}_k^{(\tau)} - \hat{p}_{k-1}^{(\tau)}\right) \\ &- \frac{2}{\bar{\rho}_{k-1} + \bar{\rho}_k} \left(\frac{g\Delta t}{2c_s^2}\right) \beta^- \left(\hat{p}_k^{(\tau)} + \hat{p}_{k-1}^{(\tau)}\right) + \frac{g\Delta t}{2} \left(\left(\frac{\hat{\theta}^\tau}{\bar{\theta}}\right)_k + \left(\frac{\hat{\theta}^\tau}{\bar{\theta}}\right)_{k-1}\right) \end{aligned} \tag{35}$$

$$\begin{aligned} \hat{p}_k^{(\tau+1)} = \hat{p}_k^{(\tau)} &- \left(\frac{c_s^2 \Delta t}{\Delta z}\right) \bar{\rho}_k \; \beta^+ \left(\hat{w}_{k'+1}^{(\tau+1)} - \hat{w}_{k'}^{(\tau+1)}\right) \\ &+ \left(\frac{g\Delta t}{2}\right) \bar{\rho}_k \; \beta^+ \left(\hat{w}_{k'+1}^{(\tau+1)} + \hat{w}_{k'}^{(\tau+1)}\right) + C_k^p \end{aligned} \tag{36}$$

with

$$\begin{aligned} C_k^p = &- \left(\frac{c_s^2 \Delta t}{\Delta z}\right) \bar{\rho}_k \; \beta^- \left(\hat{w}_{k'+1}^{(\tau)} - \hat{w}_{k'}^{(\tau)}\right) \\ &+ \left(\frac{g\Delta t}{2}\right) \bar{\rho}_k \; \beta^- \left(\hat{w}_{k'+1}^{(\tau)} + \hat{w}_{k'}^{(\tau)}\right) + \Delta t \, c_s^2 \, k \, \bar{\rho}_k \, \hat{u}_k^{(\tau+1)} \end{aligned} \tag{37}$$

for $k \in [1, ke]$.

$$\hat{\theta}_k^{(\tau+1)} = \hat{\theta}_k^{(\tau)} - \left(\frac{N^2 \, \bar{\theta}}{g}\right)_k \Delta t \left[\beta^+ \left(\frac{\hat{w}_{k'}^{(\tau+1)} + \hat{w}_{k'+1}^{(\tau+1)}}{2}\right) + \beta^- \left(\frac{\hat{w}_{k'}^{(\tau)} + \hat{w}_{k'+1}}{2}\right)\right] \tag{38}$$

for $k \in [1, ke]$.

For the application of these difference equations boundary conditions for $\hat{w}$ have to be taken into account

$$\begin{aligned} &\text{at the lower boundary:} \quad \hat{w}_1 = 0 \quad \text{and} \\ &\text{at the upper boundary:} \quad \hat{w}_{ke1} = 0 \quad \text{(lid-condition).} \end{aligned} \tag{39}$$

(It should be mentioned, that our notation is not quite consistent, since the symbol k is used to indicate both the horizontal wavenumber and a vertical gridpoint index as subscript. The physical background may, however, prevent any confusion!)

3.4 Numerical integration algorithm with an L-grid

Here, we rewrite the difference equations (32)-(39) with its implicit formulation of time differences to come to an explicit time integration process. This will be done just as demonstrated in Doms and Schättler (2002) for the LM. For the *horizontal momentum equations* (32) and (33) it follows easily

$$\hat{u}_k^{(\tau+1)} = \left(1 + \Delta t^2 \, f_0^2\right)^{-1} \left(\hat{u}_k^{(\tau)} + \Delta t \, f_0 \, \hat{v}_k^{(\tau)} - \Delta t \, \frac{k}{\bar{\rho}_k} \, \hat{p}_k^{(\tau)} \right) \tag{40}$$

$$\hat{v}_k^{(\tau+1)} = \hat{v}_k^{(\tau)} - \Delta t \, f_0 \, \hat{u}_k^{(\tau+1)} \tag{41}$$

with an additional *divergence damping* approach, where the pressure perturbation in (40) is altered:

$$\hat{p}_k^{(\tau)} := \hat{p}_k^{(\tau)} + \alpha_d \, \Delta t \, \bar{\rho}_k \, c_s^2 \left(k \, \hat{u}_k^{(\tau)} - \frac{\hat{w}_{k'+1}^{(\tau)} - \hat{w}_{k'}^{(\tau)}}{\Delta z} \right) \quad . \tag{42}$$

Due to the implicit treatment of the Coriolis terms the prognostic time-step of $\hat{u}$ is carried out first before the $\hat{v}$ - prognosis can follow.

An explicit procedure for the *vertical velocity* component must be derived next. For that purpose the pressure perturbation amplitude at the prognostic time-level $\tau + 1$, $\hat{p}_k^{(\tau+1)}$, in equation (34) is eliminated using equation (36). In the well-known manner a tri-diagonal vertical structural equation for $\hat{w}_{k'}^{(\tau+1)}$ is explicitly obtained:

$$\begin{aligned} B_2 \; \hat{w}_2^{(\tau+1)} + C_2 \; \hat{w}_3^{(\tau+1)} &= D_2^{(\tau)} \\ A_{k'} \; \hat{w}_{k'-1}^{(\tau+1)} + B_{k'} \; \hat{w}_{k'}^{(\tau+1)} + C_{k'} \; \hat{w}_{k'+1}^{(\tau+1)} &= D_{k'}^{(\tau)} \quad ; \quad k' \in \left[3, ke' - 1\right] \\ A_{ke'} \; \hat{w}_{ke'-1}^{(\tau+1)} + B_{ke'} \; \hat{w}_{ke'}^{(\tau+1)} &= D_{ke'}^{(\tau)} \end{aligned} \tag{43}$$

The right-hand side terms $D_{k'}^{(\tau)}$, at time-level τ, are known, and the time-independent coefficients $A_{k'}$,$B_{k'}$,$C_{k'}$ either. Thus, the time-extrapolated values of $\hat{w}_{k'}^{(\tau+1)}$, for $k' \in \left[2, ke'\right]$, can be determined from a Gaussian elimination process with an adherence condition at the lower boundary, $\hat{w}_1 = 0$, and a lid-condition at the upper boundary, $\hat{w}_{ke1} = 0$. The coefficients $A_{k'}$,$B_{k'}$,$C_{k'}$ and the function $D_{k'}^{(\tau)}$ in (43) read

$$A_{k'} = \left(\beta^+\right)^2 \frac{\bar{\rho}_{k-1}}{\left(\bar{\rho}_{k-1} + \bar{\rho}_k\right)/2} \left[\left(\frac{c_s\,\Delta t}{\Delta z}\right)^2 - \left(\frac{g\,\Delta t}{2c_s}\right)^2\right] = \left(\frac{\bar{\rho}_{k-1}}{\bar{\rho}_k}\right) C_{k'} \qquad \text{for } k' \in \left[3, ke'\right] \tag{44}$$

$$C_{k'} = \left(\beta^+\right)^2 \frac{\bar{\rho}_k}{\left(\bar{\rho}_{k-1} + \bar{\rho}_k\right)/2} \left[\left(\frac{c_s\,\Delta t}{\Delta z}\right)^2 - \left(\frac{g\,\Delta t}{2c_s}\right)^2\right] = \left(\frac{\bar{\rho}_k}{\bar{\rho}_{k-1}}\right) A_{k'} \qquad \text{for } k' \in \left[2, ke' - 1\right] \tag{45}$$

$$B_{k'} = 1 + 2\left(\beta^+\right)^2 \left[\left(\frac{c_s\,\Delta t}{\Delta z}\right)^2 + \left(\frac{g\,\Delta t}{2c_s}\right)^2\right] + 2\left(\beta^+\right)^2 \left(\frac{\bar{\rho}_k - \bar{\rho}_{k-1}}{\bar{\rho}_k + \bar{\rho}_{k-1}}\right) \left(\frac{g\,(\Delta t)^2}{\Delta z}\right) \qquad \text{for } k' \in \left[2, ke'\right] \tag{46}$$

$$D_{k'} = \hat{w}_{k'}^{(\tau)} - \frac{2\beta^+}{\left(\bar{\rho}_{k-1} + \bar{\rho}_k\right)} \left(\frac{\Delta t}{\Delta z}\right) \left[\left(\hat{p}_k^{(\tau)} - \hat{p}_{k-1}^{(\tau)}\right) + \left(C_k^p - C_{k-1}^p\right)\right] - \frac{2\beta^+}{\left(\bar{\rho}_{k-1} + \bar{\rho}_k\right)} \left(\frac{g\,\Delta t}{2c_s^2}\right) \left[\left(\hat{p}_k^{(\tau)} + \hat{p}_{k-1}^{(\tau)}\right) + \left(C_k^p + C_{k-1}^p\right)\right] + C_{k'}^w \qquad \text{for } k' \in \left[2, ke'\right] \tag{47}$$

with the auxiliary variables:

$$C_k^p = -\beta^-\, c_s^2 \left(\frac{\Delta t}{\Delta z}\right) \bar{\rho}_k \left(\hat{w}_{k'+1}^{(\tau)} - \hat{w}_{k'}^{(\tau)}\right) + \beta^- \left(\frac{g\,\Delta t}{2}\right) \bar{\rho}_k \left(\hat{w}_{k'+1}^{(\tau)} + \hat{w}_{k'}^{(\tau)}\right) + \Delta t\, c_s^2\, k\, \bar{\rho}_k\, \hat{u}_k^{(\tau+1)} \qquad \text{for } k \in [1, ke] \tag{48}$$

$$C_{k'}^w = -\frac{2\beta^-}{\left(\bar{\rho}_{k-1} + \bar{\rho}_k\right)} \left(\frac{\Delta t}{\Delta z}\right) \left(\hat{p}_k^{(\tau)} - \hat{p}_{k-1}^{(\tau)}\right) - \frac{2\beta^-}{\left(\bar{\rho}_{k-1} + \bar{\rho}_k\right)} \left(\frac{g\,\Delta t}{2c_s^2}\right) \left(\hat{p}_k^{(\tau)} + \hat{p}_{k-1}^{(\tau)}\right) + \left(\frac{g\,\Delta t}{2}\right) \left[\left(\frac{\hat{\theta}_k^{(\tau)}}{\bar{\theta}_k^{(\tau)}}\right) + \left(\frac{\hat{\theta}_{k-1}}{\bar{\theta}_{k-1}}\right)\right] \qquad \text{for } k' \in \left[2, ke'\right] \tag{49}$$

The Gaussian elimination procedure is then applied to (43)- (49) in a common way. By a 'top-down sweeping' the following auxiliary entities are determined first:

$$E_{ke'} := -\frac{A_{ke'}}{B_{ke'}} \qquad , \qquad F_{ke'} := \frac{D_{ke'}}{B_{ke'}} \tag{50}$$

and then for $k^{'} \in \left[ke^{'} - 1, 2\right]$:

$$\begin{aligned} E_{k'} &:= -\frac{A_{k'}}{B_{k'} + C_{k'} E_{k'+1}} \qquad , \qquad F_{k'} := \frac{D_{k'} - C_{k'} F_{k'+1}}{B_{k'} + C_{k'} E_{k'+1}} \\ E_1 &:= 0 \qquad , \qquad F_1 := \frac{D_2 - C_2 F_3}{B_2 + C_2 E_3} = \hat{w}_2^{(\tau+1)} \end{aligned} \tag{51}$$

From all following 'down-top sweeping' the vertical motion perturbation is easily calculated:

$$\hat{w}_{k'}^{(\tau+1)} = E_{k'} \hat{w}_{k'-1}^{(\tau+1)} + F_{k'} \qquad k^{'} \in \left[3, ke^{'}\right] \tag{52}$$

Once the prognostic *vertical motion perturbation* is calculated, the *pressure perturbation* and the *potential temperature perturbation* at that time-level can immediately be found from the equations ((36), (37)) and (38).

To complete the numerical integration algorithm, we list the constants how they are chosen in this model:

$f_0 = 10^{-4}\, s^{-1}$ - Coriolis parameter

$k \ = 2\pi/L$ - wavenumber associated with wavelength $L = 100, 250km$

$R \ = 287 m^2\, s^2\, K^{-1}$ - gas constant

$g \ = 9.80665 m\, s^{-2}$ - gravity constant

$c_p = 1005 J\, K^{-1}\, kg^{-1}$,

$c_v = 718 J\, K^{-1}\, kg^{-1}$ - specific heat at constant pressure and constant volume, respectively

$\varepsilon \ = 0.4$ - implicity parameter (see Subsection 3.2, (29))

$\alpha_d = 0.1, ...0.3$ - divergence damping parameter (see 3.2, (30))

$T_0 = 250K$ - assumption of an isothermal model atmosphere

$p_s = 100000Pa$ - pressure at lower boundary

$c_s^2 = \kappa\, RT_0\,, \ \ \kappa = c_p/c_v$ - constant sound wave speed squared

$\Delta t = 1s, ...10s$ - time-step

$\Delta z = (1/40)\, RT_0\, 1n\,(1000)\,/g$ - constant model layer thickness of the 40-layer model

together with formulae to calculate basic state parameters in the difference equations above

$$\bar{\rho}_k = \frac{p_s}{RT_0} \exp\left(-\frac{g}{RT_0}\, z_k\right) \;,\; \bar{\theta}_k = T_0 \exp\left(\frac{g}{c_p\, T_0}\, z_k\right)$$

$$\left(\frac{N^2\bar{\theta}}{g}\right)_k = \left(\frac{d\bar{\theta}}{d\, z}\right)_k = \frac{g}{c_p} \exp\left(\frac{g}{c_p\, T_0} z_k\right) \qquad \text{for } k \in [1, ke] \;.$$

3.5 Simulations with L-grid model version

Based on the model algorithm for a vertical L-grid, described in the previous Subsection 3.4, we carry out simulations similar to Arakawa and Konor's (1996) with their model (AKM). It serves us to calibrate our LM toy-model. Therefore, our concern is mainly to simulate hydrostatic gravity waves, which is guaranteed with the choice of relatively large horizontal wavelengths of $L = 100, 250km$ compared to the initially produced vertical wavelength. On a state of rest a local zig-zag initial perturbation in θ' is imposed to $\pm 0.5K$ at the vertical gridpoints indexed with $k = 2/3$, and $\theta' = 0$ everywhere else. From this manipulation sound- and gravity waves are generated, and their propagation can then be simulated in terms of a dispersion process. Besides linearisation, our approach differs from the leap-frog / split-explicit time-scheme of the LM in such a way, that we run the fast-mode model part in a stand-alone form not linked within a splitting scheme with the slow-mode model part. In a first set of simulations we assume a horizontal wavelength of $L = 250km$

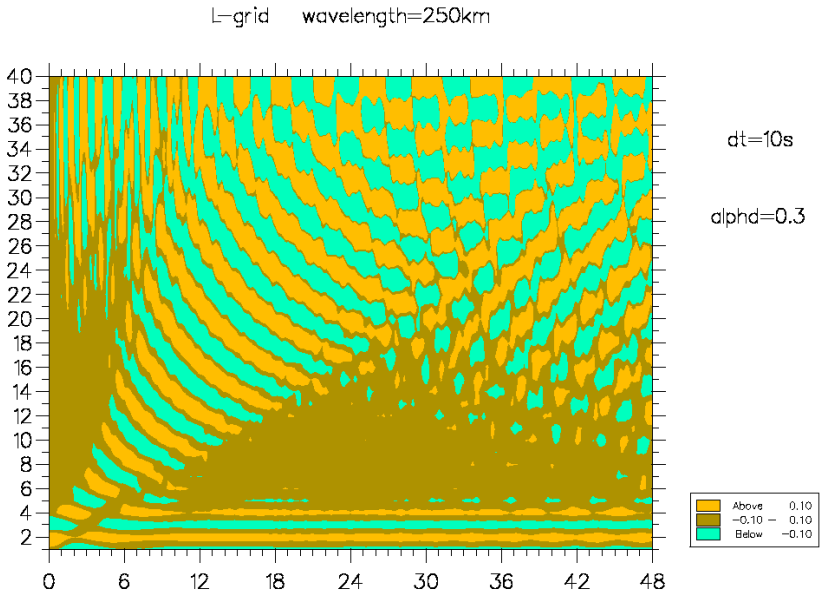

Figure 5: Linear LM fast-mode simulation with L-grid for a horizontal wave length of 250km. Time evolution of the potential temperature perturbation amplitude over 48 hours integration time with time-step $\Delta t = 10s$ and a divergence damping parameter of $\alpha_d = 0.3$ (Further explanation see text, contour interval similar to previous figures).

On an empirical ground the time-step is chosen $\Delta t = 10s$ and the divergence damping parameter has been set $\alpha_d = 0.3$ in order to damp out acoustic waves. Over 48 hours integration time the simulation shows, how a gravity wave dispersion process takes place from the assumed initial potential temperature perturbation in case of the L-grid staggering of variables and influenced by an upper lid-condition. Obviously, wave perturbations propagate only partially upward, where they are reflected at the upper boundary to reach lower parts of the integration domain again, while another wave mode remains to be stationary as a pure computational mode (Fig. 5).

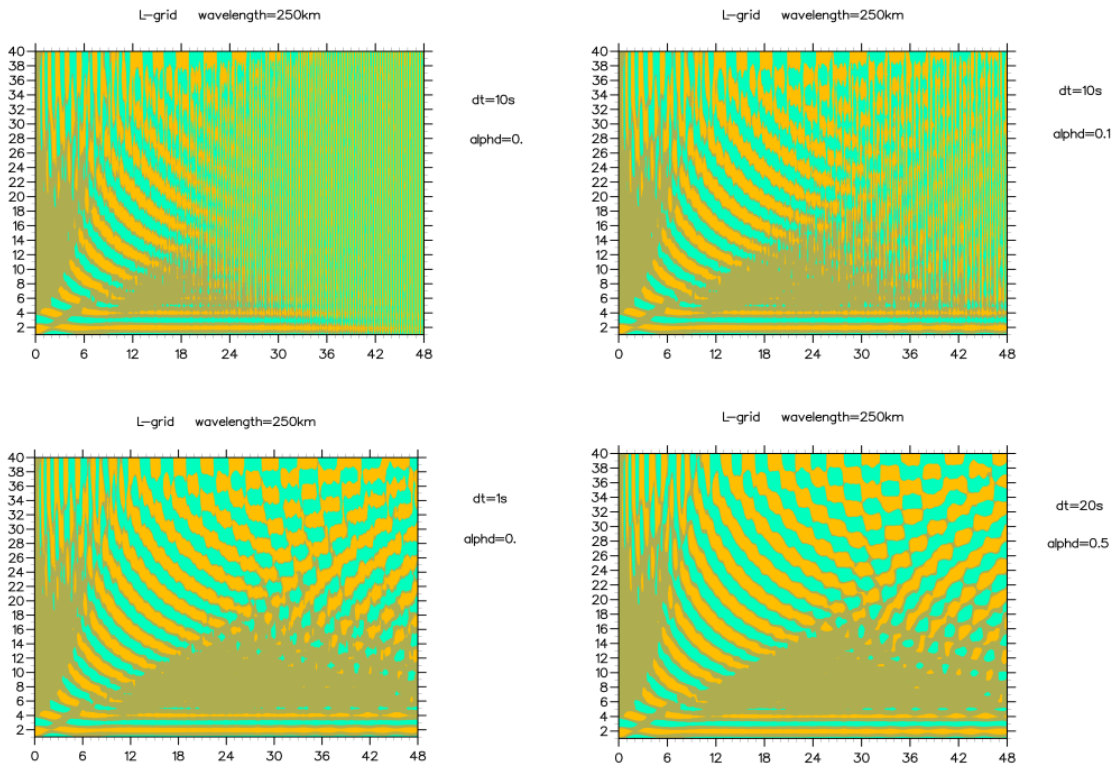

Figure 6: Further simulations with L-grid for a 250km horizontal wavelength over 48 hours integration time in dependence of varying time-step $\Delta t = 1, 10, 20s$ and divergence damping parameter of $\alpha_d = 0., 0.1, 0.5$, and compared to the simulation with $\Delta t = 10s$ and $\alpha_d = 0.3$ in Fig. 5.

From an empirical point of view the Figures 5 and 6 show that the simulation with $\Delta t = 10s$ brings about an optimal result, if the divergence damping term is switched on with $\alpha_d = 0.3$ while the choice of $\alpha_d = 0.1$ (LM-default value, see upper right panel of Figure 6) leads to an unsatisfactory solution, which tends to make the matter still worse, if $\alpha_d = 0$ (upper left panel of Figure 6) is taken. We interpret this outcome as an accuracy problem due to the choice of a time-step as large as $\Delta t = 10s$. Related truncation errors seem to become the cause of artificial, horizontally propagating acoustic waves, which however can be damped, if the divergence damping mechanism is taken into account. Due to this, the choice of $\alpha_d = 0.3$ is shown to be sufficient, while $\alpha_d = 0.1$ is still too small to be effective. In the lower right panel of Figure 6 it is shown that even with a time-step of $\Delta t = 20s$, which is connected with a still more reduced time-difference accuracy, the simulation becomes successful, provided the divergence damping effect is sufficiently increased (e.g. $\alpha_d = 0.5$). If in contrast to this the time-difference accuracy is improved by using a sufficiently small time-step of $\Delta t = 1s$ there seems to be no reason to apply any divergence damping, since no spurious acoustic waves occur (lower left panel in Figure 6). Here we speculate about the nature of this kind of time-difference accuracy. From a physical point of view, an inherent hydrostatic adjustment process seems to take place, where the horizontally propagating acoustic modes play the role of a catalyst. If the timestep is small enough, the simulation is accurate to model the adaptation well enough in analogy to the well-known geostrophic adjustment, which must be simulated properly to avoid noisy gravity waves. This means here that larger timesteps appear to produce spurious acoustic waves which are then necessery to be damped out using some remedy in terms of an stronger divergence damping parameter. The same qualitative result can also be shown from simulations with a horizontal wavelength of $L = 100km$ for the assumed initial potential temperature perturbation (Figure 7). With $\Delta t = 1s$ and $\alpha_d = 0.3$ one obtains an optimal result, while with the same time-step, but ignored

divergence damping, the solution tends to become noisy. If then the time-step is further increased up to $\Delta t = 5s$ the emergence of spurious horizontally propagating acoustic waves is obvious, and the gravity wave solution is almost destroyed. The choice of an increased divergence damping parameter, $\alpha_d = 0.5$, makes, however, this larger time-step applicable and leads to a solution comparable with that from $\Delta t = 1s$ and $\alpha_d = 0.3$. With the specific time-differencing scheme suitable, and applied here to the compressible nonhydrostatic equations, we were able to recover the hydrostatic gravity wave solutions for a 100km- and 250km horizontal wavelength as found from the hydrostatic AKM concerning the L-grid. This has been demonstrated by comparing the appropriate solutions of Figure 2 with those of Figures 5 , 6 and 7 . Of particular interest is here, too, that the L-grid causes an unwanted stationary zigzag-computational mode which we know to be avoided in the AKM when introducing the CP-grid staggering instead. This change to the CP-grid must be managed in the following for our toy-model.

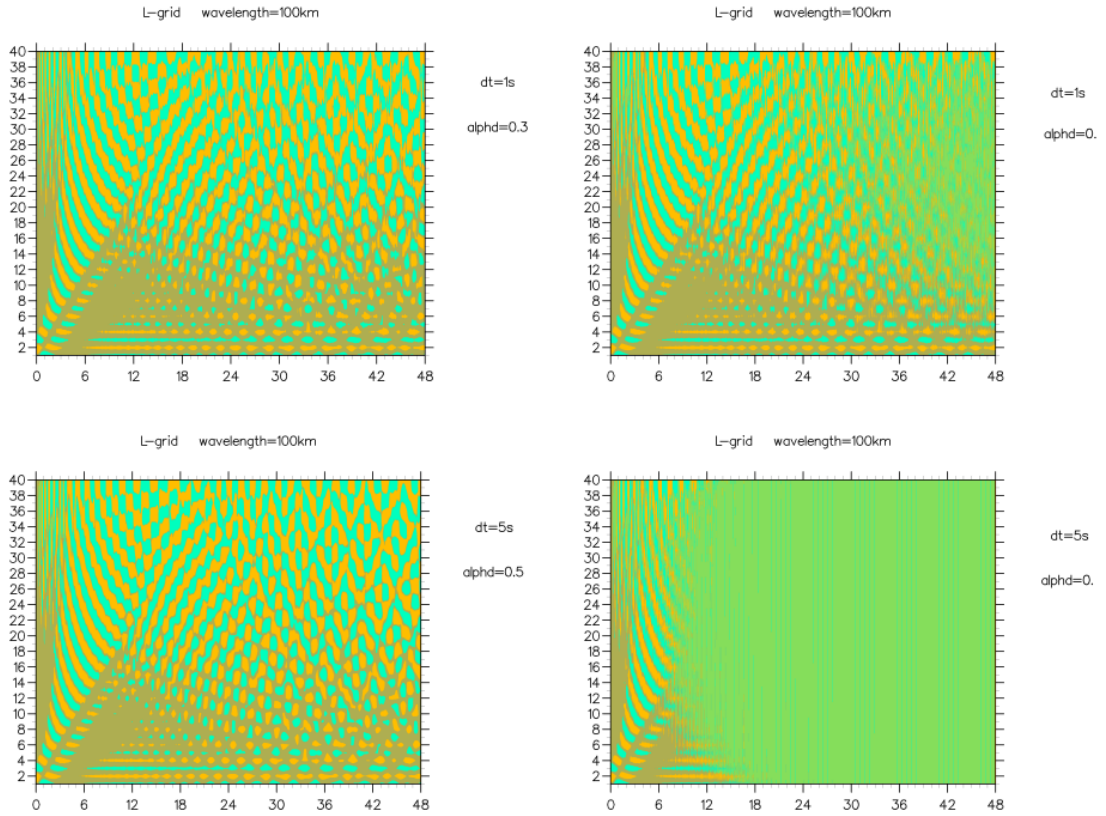

Figure 7: Simulations with L-grid for a 100km horizontal wavelength over 48 hours integration time for time steps $\Delta t = 1s$ and $5s$ in dependence of divergence damping parameter of $\alpha_d = 0., 0.3, 0.5$.

3.6 Vertical grid-staggering with a CP-grid

We refer strictly to our description of the L-grid algorithm in Subsections 3.3 and 3.4 . In order to define here the vertical differencing for a CP-grid option of the LM fast-wave toy-model, we need only list the differences to the L-grid formulation. In contrast to the L-grid scheme (see Figure 4) the CP-grid staggering scheme is shown in Figure 8.

In this case the variables $\hat{u}$, $\hat{v}$, $\hat{p}$ are placed at main-levels indicated with indices $k \in [1, k]$, while $\hat{w}$ and $\hat{\theta}$ are defined at half-levels indexed with $k^{'} \in [1, ke1]$. For the basic state we assume again $\bar{\rho}$ to be positioned at main-levels, but $\bar{\theta}$ now at half-levels together with its perturbation value $\hat{\theta}$. To make the

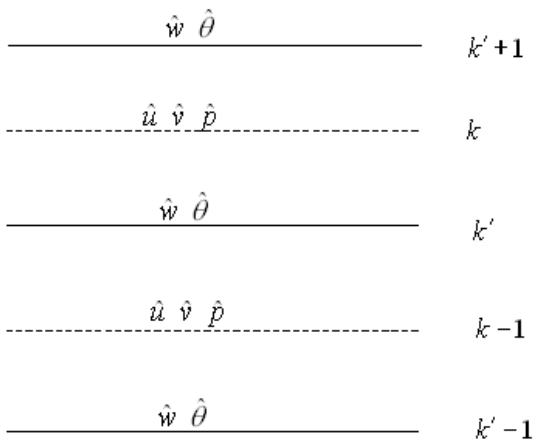

Figure 8: Scheme of vertical staggering according to CP-grid

matter simple enough, we comment here only the changes from the numerical integration algorithm written down in the Subsection 3.4 for the L-grid. The horizontal momentum equations (40), (41) with the divergence damping (42) included remain as they stand there. The Gaussian elimination procedure to compute the vertical velocity from a tri-diagonal vertical structural equation system (43) remains also formally untouched . Only the term $C^w_{k'}$ involved, obtains a more simple form compared to (49). Due to a more natural formulation of the buoyancy term with a CP-grid, its vertical averaging is avoided. Instead of (35) we have

$$C^w_{k'} = \ldots \quad g\Delta t \left(\frac{\hat{\theta}^{(\tau)}}{\bar{\theta}} \right)_{k'} \qquad \text{for} \quad k' \in \left[2, ke' \right] \tag{53}$$

The first two terms on the right-hand side of equation (35)/(49) are identically introduced in (53) written in symbolic form by dots. The pressure perturbation equation ((36), (37)) is used without any change, while a minimal modification is made for the potential temperature perturbation equation (38):

$$\hat{\theta}^{(\tau+1)}_{k'} = \hat{\theta}^{(\tau)}_{k'} - \left(\frac{N^2 \bar{\theta}}{g} \right)_{k'} \Delta t \left(\beta^+ \hat{w}^{(\tau+1)}_{k'} + \beta^- \hat{w}^{(\tau)}_{k'} \right) \qquad \text{for} \quad k' \in [1, ke1] \tag{54}$$

The boundary conditions (39) are assumed here, too, and the list of constants used in the L-grid version is also valid. With this specifications we are going to carry out similar simulations with the CP-grid model version to show the impact of the CP-grid against the L-grid as already demonstrated with the hydrostatic AKM in Section 2.

3.7 Simulation with the CP-grid model version

Here we carry out simulations on the basis of the CP-grid model version described in Subsection 3.6 . With reference to 3.5, the numerical set-up is chosen to compare the results with the previous L-grid simulations. For horizontal wavelengths $L = 100, 250km$ with time-step $\Delta t = 1s$ and $10s$, respectively, and $\alpha_d = 0.3$ in each case, the CP-grid results are shown in Figure 9, compared with the corresponding L-grid simulations over 48 hours integration time. This result can be compared with that in Figure 2, where analogous runs have been shown with the hydrostatic AKM. The similarity of results between Figure 2 and Figure 9 was expected to be found in this way, because in both situations

hydrostatic gravity waves were simulated due to the same, relatively long horizontal wavelengths of the assumed initial perturbation. Therefore, the discussion of the results depicted in Figure 9 is qualitatively the same as that about Arakawa and Konor's simulation shown in Figure 2, and need not be repeated here. So we can refer to our discussion in Section 2. On the whole, we can state that a computational mode in the L-grid nonhydrostatic model version is possible to occur - here deliberately provoked by a special initial perturbation - and due to the introduction of a CP-grid instead this unphysical nuisance is removed, and, moreover, we observe that the CP-grid seems to support the gravity wave dispersion process much better.

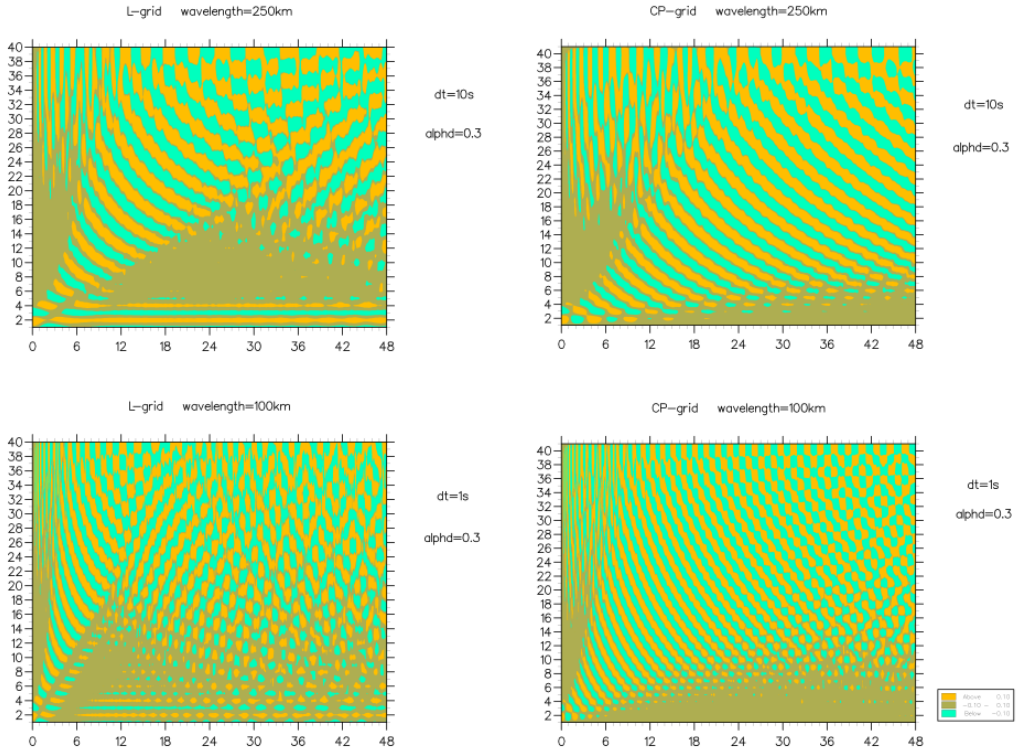

Figure 9: Comparison of L-grid simulations with corresponding CP-grid runs for horizontal wave components with $L = 100, 250km$ wave length over 48hours integration time.

In order to demonstrate further aspects of the possible occurrence of a computational mode in the L-grid, Arakawa and Konor (1996) carried out still a second set of simulations with their AKM not mentioned up to now in this paper. We will add this in brief from the point of view of the LM toy-model. In this set, the initial conditions are modified in a way that $\theta^{'} = 0$ is assumed everywhere without any local perturbation imposed. Instead, a Newtonian-type diabatic heating term is added in the prognostic equation for $\hat{\theta}$, (20), on its right-hand side, using a time-independent equilibrium value amplitude $\hat{\theta}^*$. The modified potential temperature equation reads then

$$\frac{\partial \hat{\theta}}{\partial t} = -\frac{N^2 \bar{\theta}}{g}\,\hat{w} - \lambda\,\left(\hat{\theta} - \hat{\theta}^*\right) \tag{55}$$

with $\hat{\theta}^* = 10K$ for the equilibrium value, and $\lambda = 1/86400\,s^{-1}$ for the relaxation constant. This term is applied at only one single model level, at $k = 4$ and $k^{'} = 4$, respectively. These parameters are identical with those in Arakawa and Konor's paper. In Figure 10 we show the corresponding results from this set of simulations.

The simulation with the horizontal wavelength of 250 km is not shown here. It brings qualitatively

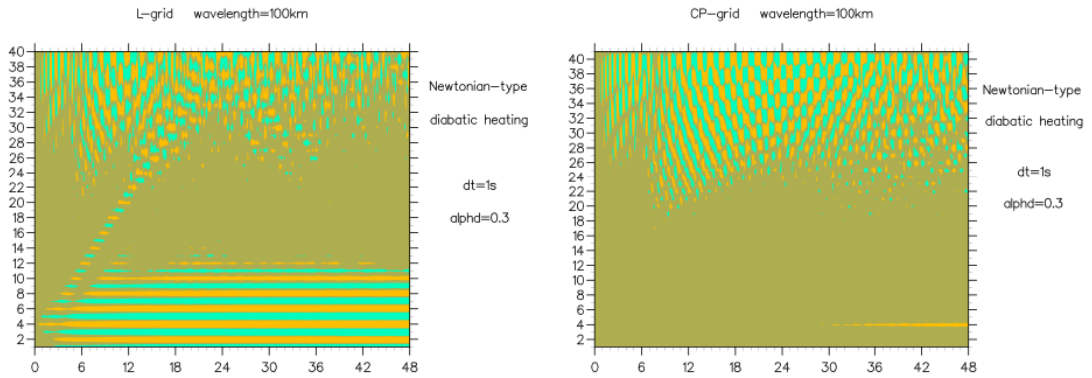

Figure 10: Simulation with Newtonian-type heat forcing at a single model level for horizontal wavelength of 100km and L-grid against CP-grid.

an analogous result as shown for the 100km-wave component. Since for both these large wavelengths the nonhydrostatic model simulates wave solutions comparable with the hydrostatic approximation, the results can be compared directly with the corresponding AKM-simulations (see Figure 4 in Arakawa and Konor 1996). Thus, the same qualitative discussion of the result in Figure 10 is valid and, with reference to Arakawa and Konor (1996), needs not be repeated here. In particular, we see the generation of a spurious zigzag distribution of the potential temperature perturbation due to the L-grid, which does not occur when using the CP-grid instead. We add still another experiment, where the effect of a subgrid-scale convective forcing is simulated with the given toy-model. For that purpose the continuity equation is thought to be extended to take into account an additional term describing the divergence of a subgrid mass flux. In terms of equation (19), which is the continuity equation for the given system, we add an expression of the vertical divergence of a vertical mass flux like this:

$$\frac{\partial \hat{p}}{\partial t} = g\bar{\rho}\,\hat{w} - c_s^2\,\bar{\rho}\left(\frac{\partial \hat{w}}{\partial z} - k\hat{u}\right) - c_s^2\,\frac{\partial \hat{F}_z}{\partial z} \tag{56}$$

With background values $w^{'} \sim 5m\,s^{-}1$, $\rho^{'} \sim 10^{-3}kg\,m^{-3}$, $\Delta z \sim 10^3 m$ we make use of an estimate

$$\left|c_s^2\,\partial\,\hat{F}_z/\partial z\right| \sim 0.5kg\,m^{-1}\,s^3 \qquad .$$

The positive value is imposed at an altitude corresponding to level $k = 3$, while its negative value holds at $k = 8$. Otherwise this term is set equal zero. Thus, a step-like vertical distribution of an constant mass flux directed upward in between an interval $3 \leq k \leq 8$ is imposed, while it is zero below and above. In the simulation with this kind of forcing the term of concern is assumed to be constant in time. In this experimental set-up no initial local perturbation is otherwise imposed.

Due to this specification of a vertical massflux distribution the following result is expected: massflux divergence (convergence) is accompanied with flow convergence (divergence) at $k = 3$ ($k = 8$). Thus, we observe at $k = 8$ downward motion of air with higher θ from above, which leads to local heating there, while upward motion right next at $k = 9$ carries air with lower θ from below bringing local cooling. The same takes place at $k = 3$, and $k = 4$, respectively, but in reverse order and somewhat weaker. As demonstrated in Figure 11, the typical difference of simulation results between L-grid and CP-grid is observed. The L-grid produces a stationary computational zig-zag structure, while the physical solution expected cannot be reproduced. The CP-grid, however, avoids this non-physical phenomenon and seems even necessary to properly simulate the adopted process.

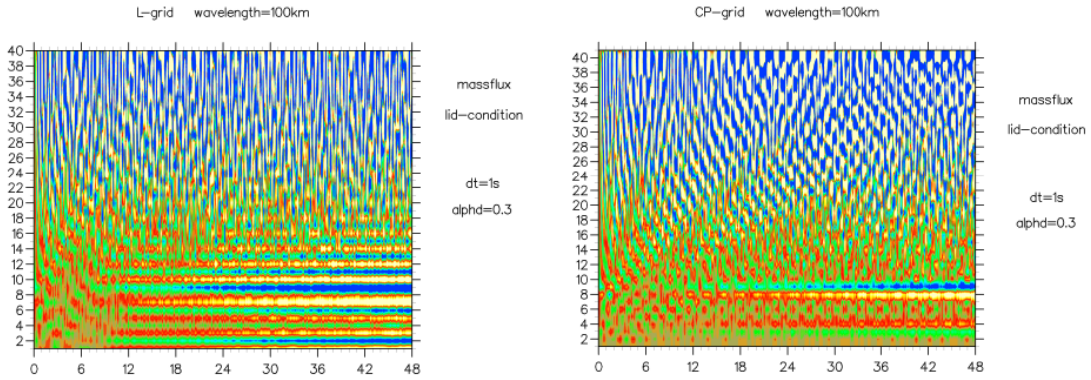

Figure 11: Time evolution of the potential temperature perturbation with imposed subgrid-scale massflux (see text) for horizontal wavelength of 100km with L-grid versus CP-grid. (contour colour interval here 0.01K in between (-0.1; + 0.1).

In all Figures above the simulation results have been shown over the entire integration domain. There we have always tacitly accepted that the internal gravity wave pattern propagating upward arrive eventually at the upper model boundary, where they are reflected owing to the assumed lid-condition $\hat{w}_{top} = 0$ with a following contamination of the physical solution. These results suggest urgently the implementation of an absorbing upper boundary condition instead of the reflective lid-condition here still applied. This will be our concern in the next section.

4 Application of a radiative upper boundary condition

In all our results shown by now it can be observed that reflecting wave components occur which propagate downward as an unnatural phenomenon to contaminate then internal solutions, and, moreover, veil and distort even unphysical modes like zigzag patterns owing to an L-grid which might then not always be detected easily from. With this motivation, but also from much more general reasons, it is strongly indicated to improve any model of concern in order to get rid of an upper lid-condition and introduce an absorbing or non-reflecting upper condition instead. Here, we are interested in applying a radiative boundary condition for our compressible nonhydrostatic toy-model as a desirable improvement in the above sense. Moreover, we have in mind to start finding out in principle a way to extend this application to the real LM. In the following Section, however, we deal with that problem in the narrow sense. It needs no explanation, why we are here particularly interested in applying a radiative boundary condition, since our toy-model is a simple horizontally spectral model. Thus, we operate always in the Fourier space with a monochromatic wave component which allows the direct application of a radiative boundary condition, while normally a Fourier transform is necessary to apply.

4.1 Derivation of the Klemp-Durran-Bougeault type of a radiative upper boundary condition

The following analysis starts from the toy-model equations (16) - (20) with all their explanations given in Section 3. The only modification is thought to be done in the prognostic $\hat{w}$ - equation, where a hydrostatic switch μ is added to be multiplied with the vertical acceleration term in (18). Setting $\mu = 1$ gives the full nonhydrostatic system while $\mu = 0$ reduces the system to the hydrostatic model equations. With this notation we carry out the elimination of the horizontal momentum components and the potential temperature perturbation amplitude to obtain two relationships for pressure and vertical momentum:

$$\left[\frac{1}{c_s^2}\left(\frac{\partial^2}{\partial t^2}+f_0^2\right)+k^2\right]\frac{\partial \hat{p}}{\partial t}=-\left(\frac{\partial^2}{\partial t^2}+f_0^2\right)\left(\frac{\partial}{\partial z}+\frac{N^2}{g}\right)(\bar{\rho}\hat{w}) \tag{57}$$

$$\left(\frac{\partial}{\partial z}+\frac{g}{c_s^2}\right)\frac{\partial \hat{p}}{\partial t}=-\left(\mu\frac{\partial^2}{\partial t^2}+N^2\right)(\bar{\rho}\hat{w}) \tag{58}$$

The z- and t- dependencies may now be separated

$$\begin{pmatrix}\hat{p}\\ \bar{\rho}\hat{w}\end{pmatrix}=\mathrm{Re}\begin{pmatrix}P(z)\\ W(z)\end{pmatrix}\exp(-i\omega t) \tag{59}$$

allowing the following to be written:

$$\left[\frac{\partial^2}{\partial z^2}+\left(\frac{g}{c_s^2}+\frac{N^2}{g}\right)\frac{\partial}{\partial z}+\frac{N^2}{c_s^2}\right]\begin{pmatrix}P\\ W\end{pmatrix}+\left(\frac{N^2-\mu^2\omega}{\omega^2-f_0^2}\right)\left(k^2-\frac{\omega^2-f_0^2}{c_s^2}\right)\begin{pmatrix}P\\ W\end{pmatrix}=0 \tag{60}$$

Normalising equation (60), the change of variables is made

$$\begin{pmatrix}P(z)\\ W(z)\end{pmatrix}=\begin{pmatrix}\tilde{P}(z)\\ \tilde{W}(z)\end{pmatrix}\exp\left(-\frac{z}{2H}\right) \tag{61}$$

using the definition of a reciprocal vertical scale height

$$\frac{1}{H} = -\frac{1}{\bar{\rho}}\frac{d\bar{\rho}}{dz} = \frac{N^2}{g} + \frac{g}{c_s^2} \qquad , \tag{62}$$

finally leaves the well-known wave equation

$$\frac{d^2}{d\,z^2}\begin{pmatrix}\tilde{P}\\ \tilde{W}\end{pmatrix} + n^2\begin{pmatrix}\tilde{P}\\ \tilde{W}\end{pmatrix} = 0 \tag{63}$$

with the vertical wavenumber squared

$$n^2 = \frac{\left(N^2 - \mu^2\omega^2\right)k^2}{\omega^2 - f_0^2} + \frac{\mu^2\omega^2}{c_s^2} - \frac{1}{4H^2} \tag{64}$$

The general solution of (63) reads

$$\tilde{W}\,(z) = a\,\exp\left(i\,n\,z\right) + b\,\exp\left(-i\,n\,z\right) \tag{65}$$

and similar for $\tilde{P}\,(z)$. The relationship (64) constitutes a rather general dispersion equation to determine the frequency ω for acoustic and inertia-gravity modes. A fairly detailed discussion for $\mu = 1$ can be found in Gossard and Hooke (1975, p. 112). In a next step we are interested in considering the vertical energy flux averaged over a periodic time length $2\pi/\omega$. For the present we find

$$\begin{aligned}\overline{\hat{p}\hat{w}} = \overline{\mathrm{Re}\left(P\exp\left(-i\omega t\right)\right)\mathrm{Re}\left(\frac{W}{\bar{\rho}}\exp\left(-i\omega t\right)\right)} &= \frac{1}{4\bar{\rho}}\left(P\overset{*}{W} + \overset{*}{P}W\right)\\ &= \frac{1}{2\bar{\rho}\,(0)}\mathrm{Re}\left(\overset{*}{\tilde{W}}\tilde{P}\right)\end{aligned} \tag{66}$$

The upper stars in (66) denote complex-conjugate entities. This general expression needs to be more specified in view of introducing now the Klemp-Durran-Bougeault radiative boundary condition (= KDB-RUBC) with its rather restricting assumptions. We are motivated to do so, since it is common that a radiative boundary condition following from the general case is impracticable to be applied due to its global properties in space and time. In contrast, the KDB-RUBC seems here particularly attractive, because it is local in time, and the global character in space is not an obstacle at all due to the specific definition of model variables. The list of assumptions to arrive at the KDB-RUBC is:

- hydrostatic approximation $(\mu = 0)$
- anelastic condition $\left(c_s^2 \to \infty\right)$
- isothermal basic state
- no rotation $(f_0 = 0)$ (67)
- Boussinesq - approximation $\left(\frac{\partial}{\partial z} \gg \frac{1}{H}, n^2 \gg \frac{1}{H^2}\right)$

With this limitations the dispersion equation reduces to

$$\omega n = \pm N\, k \tag{68}$$

and from (57) follows with (59) and (61) the relation

$$\tilde{P} = i\frac{\omega}{k^2}\frac{d\tilde{W}}{dz} \qquad . \tag{69}$$

Inserting (69) in (66) leads, together with (65), to

$$\overline{\hat{p}\hat{w}} = -\frac{\omega n}{2\bar{\rho}_0 k^2}\left(|a|^2 - |b|^2\right) \tag{70}$$

At this point we have to specify the energy flux (70) at the upper boundary. In accordance with a condition of outgoing wave energy there, it is inferred from the energy budget equation (21) by integration from the bottom to the upper boundary that

$$\overline{(\hat{p}\hat{w})}_{top} > 0 \tag{71}$$

must hold. With always $n > 0$ (cf. with (65)) we start assuming $\omega n = Nk > 0$. In accordance with the desirable condition (71) it follows from (70) at the upper boundary $a = 0$. In this case we infer from (65) $d\tilde{W}/dz = -in\tilde{W}$, and via (69) we arrive at

$$\tilde{P}_{top} = \frac{N_{top}}{k}\tilde{W}_{top} \qquad . \tag{72}$$

If, however, $\omega n = -N\, k < 0$, we find with $b = 0$ from (65), (69), (70) the same result as (72). Provided that $z_{top} < \infty$, we finally obtain by use of (61) and then ((57), (58)) the KDB-RUBC in the form

$$\hat{p}_{top} = \frac{(\bar{\rho}N)_{top}}{k}\hat{w}_{top} \qquad . \tag{73}$$

In our case $k > 0$ is always valid. A direct application of (73) would be possible in our toy-model, provided the limiting assumptions behind this RUBC can be neglected compared to its desirable advantages. Apart from the original references (Klemp and Durran 1983, Bougeault 1983) we refer particularly to Durran (1999) who gave in his monography an excellent overview about this subject. Moreover, Durran has suggested an interesting computational method, how to incorporate the KDB-RUBC in a nonhydrostatic linear model algorithm. In the following we want to take up with his idea in order to apply it for the present model scheme.

4.2 Implementation of the KDB - RUBC

Before we put forward the matter, it seems worth thinking about, if there is really a good reason to deal with the KDB-RUBC in connection with a compressible nonhydrostatic model because of rather limited assumptions implied in this boundary condition. We are motivated to do so because of a reasoning as follows. The time differencing scheme used and described in Section 3.2, which

is essentially the time scheme in the fast-wave part of the LM, treats those terms responsible for vertically propagating acoustic waves implicitly in order to damp them significantly. Moreover, the divergence damping modifying the horizontal pressure gradient term serves to damp acoustic waves, so that, on the whole, acoustic modes seem to be significantly removed, while gravity modes, as the essential physical content of this equation part, remain untouched due to these numerical techniques. Having almost only gravity modes involved in this scheme we want to make, in addition, sure the applicability of the KDB-RUBC by treating approximately hydrostatic gravity waves (which makes then the solution comparable with the simulations from Arakawa and Konor who used a hydrostatic system). In this line we carry out a special simulation with our toy-model stipulating now $k = 0$ for an infinite horizontal wavelength and the case of no rotation, $f_0 = 0$. The model is initialised again with the above defined zigzag-perturbation for $\hat{\theta}$ with $\pm 0.5K$ at vertical gridpoints indexed with k=2 and k=3, respectively. In contrast to the complete equation system (16) - (20) the reduced one leads instead of the dispersion relations (22) and (23) here to a stationary gravity solution $\omega_g^2 = 0$ and to acoustic wave modes propagating vertically only, $\omega_a^2 \approx c_s^2\, n^2$. This simulation is shown in Figure 12. It supports the possible application of the KDB-RUBC.

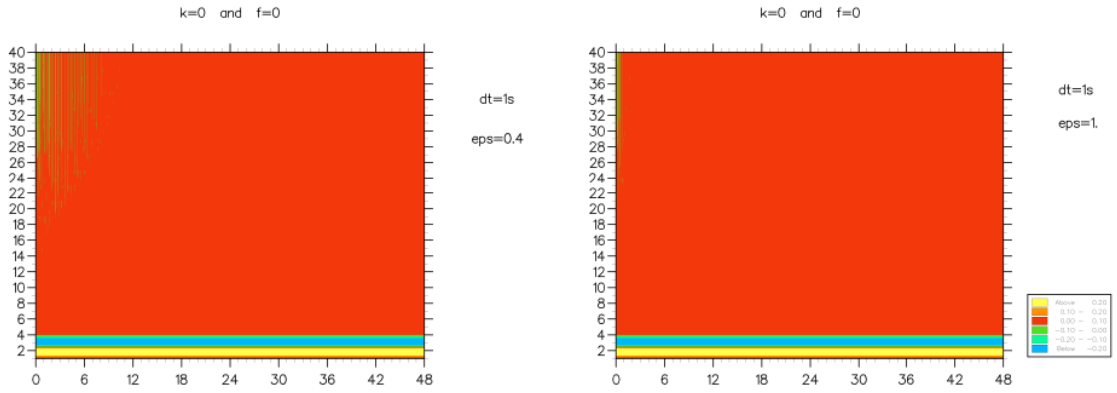

Figure 12: No rotation case simulation over 48 hours integration time with zero horizontal wavenumber. Lower stripe demonstrates a stationary gravity mode with no dispersion at all in both panels. Vertically propagating acoustic waves are treated implicitly, in the left panel with $\varepsilon = 0.4$, and in the right panel fully implicit with $\varepsilon = 1$. (plot valid both for L- and CP-grid).

Figure 12 demonstrates that the propagation of gravity modes have been suppressed. The local initial potential temperature perturbation can therefore not trigger a dispersion process compared to the more general toy-model simulations discussed above. Instead, the initial zig-zag perturbation remains so during the integration owing to a stationary mode, $\omega_g^2 = 0$. Due to the existence of a vertically propagating acoustic mode we can, however, test how the implicit time-scheme does work to damp off this mode in dependence of the implicity parameter ε. In an isolated manner we can observe that with the LM default-value $\varepsilon = 0.4$, that is with the implicity weights $\beta^+ = 0.7$ and $\beta^- = 0.3$, the acoustic mode, also caused by the special initial perturbation, is significantly reduced and eventually totally removed. In case of a fully implicit treatment ($\varepsilon = 1$, that corresponds to $\beta^+ = 1$ and $\beta^- = 0$) the effect of filtering out the acoustic mode is still more obvious. Since the implicit technique seems sufficient to remove vertically propagating acoustic waves, we conclude that the introduction of the KDB-RUBC, exclusively effective for (hydrostatic) gravity modes, may be possible to be used also in a nonhydrostatic compressible model frame provided that acoustic modes are sufficiently removed by appropriate numerical methods. From this thinking we are motivated to apply the KDB-RUBC in the given model. We start from the model equations with the given time- and vertical differencing scheme, described above in Subsection 3.2, 3.3 and 3.4 (equations (24) - (30), (31) - (39), and more directly, equations (40) - (51)). To demonstrate the method, we use the

vertical L-grid version first. The adaptation to the CP-grid is then easy to be done. Fortunately, a *first method* how to accomplish our approach, has been proposed by Durran (1999, p.429-430), which seems encouraging to be adopted for our purpose.

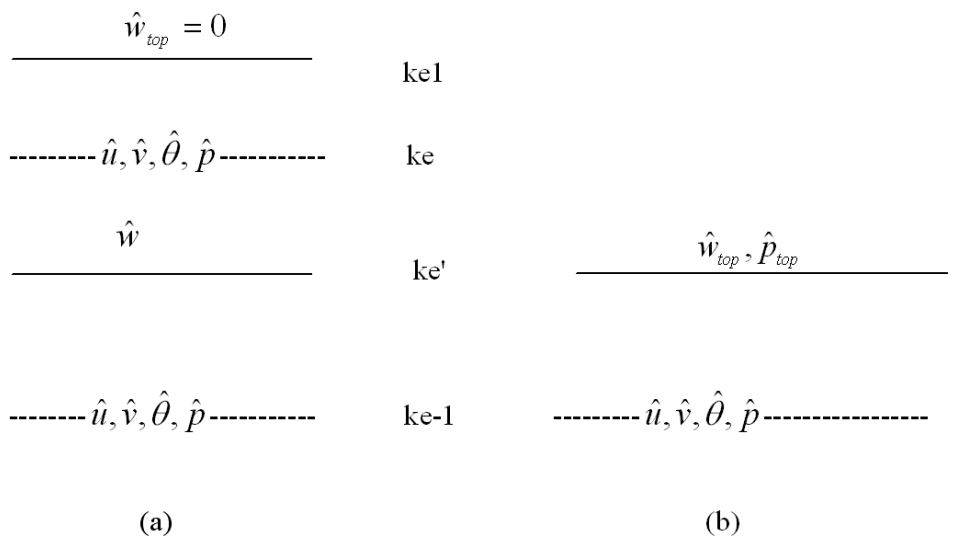

Figure 13: Change of uppermost gridpoint placement from case with (a) upper lid-condition to case (b) for introducing an RUBC according to Durran's (1999) approach.

According to Durran (1999), we change the numerical integration algorithm shown in Subsections 3.3 and 3.4 as follows. As indicated in Figure 13, we reduce the number of vertical computational gridpoints from ke to $ke-1$. Thus, the horizontal momentum equations ((40), (41)), with (42) involved, the pressure perturbation equation (27) and the potential temperature equation (28) are applied at vertical gridpoints $k \in [1, ke-1]$. With these difference equations for $k = ke-1$ there is, in particular, an access to $\hat{w}_{ke'}^{(\tau,\tau+1)} = \hat{w}_{top}^{(\tau,\tau+1)}$ which appears to be now the non-zero upper boundary value. Durran's approach consists then in changing in the tri-diagonal structural equation set for $\hat{w}_{k'}^{(\tau+1)}$, (43), the latter equation for $k = ke^{'}$. This will be elaborated next. We start from the prognostic $\hat{w}_{k'}^{(\tau+1)}$ - equation (34) which must be reformulated for $k = ke^{'}$ in such a way that an access to $\hat{p}_{ke}^{(\tau,\tau+1)}$ is avoided. This is made by using forward differences for the corresponding terms in (34) together with (35), where we define a new pressure value at the half-indexed gridpoint $k^{'} = ke^{'}$, $\hat{p}_{ke'}^{(\tau,\tau+1)} = \hat{p}_{top}^{(\tau)}$. This becomes necessary due to the proportionality of spectral perturbation pressure and vertical motion in the KDB-RUBC (73). So we have

$$\begin{aligned}\hat{w}_{top}^{(\tau+1)} = \hat{w}_{top}^{(\tau)} &- \frac{4}{\bar{\rho}_{ke-1}+\bar{\rho}_{ke}}\left(\frac{\Delta t}{\Delta z}\right)\beta^{+}\left(\hat{p}_{top}^{(\tau+1)} - \hat{p}_{ke-1}^{(\tau+1)}\right) \\ &- \frac{2}{\bar{\rho}_{ke-1}+\bar{\rho}_{ke}}\left(\frac{g\Delta t}{c_s^2}\right)\beta^{+}\hat{p}_{top}^{(\tau+1)} + C_{top}^{w}\end{aligned} \tag{74}$$

with a similar change in C_{top}^{w}:

$$\begin{aligned}C_{top}^{w} = -\frac{4\beta^{-}}{\bar{\rho}_{ke-1}+\bar{\rho}_{ke}}\left(\frac{\Delta t}{\Delta z}\right)\left(\hat{p}_{top}^{(\tau)} - \hat{p}_{ke-1}^{(\tau)}\right) &- \frac{2\beta^{-}}{\bar{\rho}_{ke-1}+\bar{\rho}_{ke}}\left(\frac{g\Delta t}{c_s^2}\right)\hat{p}_{top}^{(\tau)} \\ &+ \frac{g\Delta t}{2}\left(\frac{\hat{\theta}_{ke-1}}{\bar{\theta}_{ke}} + \frac{\hat{\theta}_{ke-1}}{\bar{\theta}_{ke-1}}\right)\end{aligned} \tag{75}$$

and some reasonable approximation for the latter term in (75). In the next step, equation (36) for $k = ke - 1$ is used to eliminate $\hat{p}_{ke-1}^{(\tau+1)}$ from equation (74) which leads in contrast to the general procedure of Subsection 3.4 to a more specific relationship

$$A_{top}\hat{w}_{ke'-1}^{(\tau+1)} + B_{top}\hat{w}_{top}^{(\tau+1)} = D_{top}^{(\tau)} - \tilde{\alpha}_{top}\hat{p}_{top}^{(\tau+1)} \tag{76}$$

with coefficients A_{top}, B_{top}, differing from the former $A_{ke'}$, $B_{ke'}$ in (43), and with an additional coefficient $\tilde{\alpha}_{top}$:

$$A_{top} = -\left(\beta^{+}\right)^{2} \frac{\bar{\rho}_{ke-1}}{\left(\bar{\rho}_{ke-1} + \bar{\rho}_{ke}\right)/2} \left[2\left(\frac{c_s \Delta t}{\Delta z}\right)^{2} + g\frac{(\Delta t)^{2}}{\Delta z}\right] \tag{77}$$

$$B_{top} = 1 + \left(\beta^{+}\right)^{2} \frac{\bar{\rho}_{ke-1}}{\left(\bar{\rho}_{ke-1} + \bar{\rho}_{ke}/2\right)} \left[2\left(\frac{c_s \Delta t}{\Delta z}\right)^{2} - g\frac{(\Delta t)^{2}}{\Delta z}\right] \tag{78}$$

$$\tilde{\alpha}_{top} = \frac{4\beta^{+}}{\left(\bar{\rho}_{ke-1} + \bar{\rho}_{ke}\right)} \left[\left(\frac{\Delta t}{\Delta z}\right) + \left(\frac{g\Delta t}{2c_s^{2}}\right)\right] \tag{79}$$

The right hand side term $D_{top}^{(\tau)}$ reads

$$D_{top}^{(\tau)} = \hat{w}_{top}^{(\tau)} + 4\beta^{+} \frac{(\Delta t/\Delta z)}{\left(\bar{\rho}_{ke-1} + \bar{\rho}_{ke}\right)} \left(\hat{p}_{ke-1}^{(\tau)} + C_{ke-1}^{p}\right) + C_{top}^{w} \tag{80}$$

Here we arrive at a point, where the KDB-RUBC (73) needs to be introduced explicitly. We use it in the form

$$\hat{p}_{top}^{(\tau+1,\tau)} = \left(\frac{N\bar{\rho}}{k}\right)_{top} \hat{w}_{top}^{(\tau+1,\tau)} \qquad \Rightarrow \qquad b_{top}\ \hat{w}_{top}^{(\tau+1,\tau)} \tag{81}$$

with the definition

$$b_{top} := \left(\frac{N\bar{\rho}}{k}\right)_{top} = \frac{g\sqrt{\kappa - 1}}{2c_s k}\left(\bar{\rho}_{ke-1} + \bar{\rho}_{ke}\right) \quad , \quad \kappa = c_p/c_v \tag{82}$$

for the assumed isothermal basic state. The KDB-RUBC ((81) , (82)) is then inserted in (76) to eliminate $\hat{p}_{top}^{(\tau+1)}$. In contrast to the Gaussian elimination procedure in Subsection 3.4, the 'top down sweeping' for the auxiliary entities $E_{k'}$, $F_{k'}$ begins here instead of (50) with

$$E := -\frac{A_{top}}{B_{top} + \tilde{\alpha}_{top} b_{top}} \qquad and \qquad F_{ke'} := -\frac{D_{top}}{B_{top} + \tilde{\alpha}_{top} b_{top}} \tag{83}$$

while the other entities for $k^{'} \in \left[ke^{'} - 1, 2\right]$ remain unchanged as in (51). It should be noticed that $\hat{p}_{top}^{(\tau)}$ in C_{top}^{w} is eliminated by using ((81) , (82)) either. The following 'down-top sweeping' to calculate the vertical motion $\hat{w}_{k'}^{(\tau+1)}$ for $k^{'} \in \left[3, ke^{'}\right]$ is then accomplished according to (52). The prognostic step for the pressure perturbation and also for the potential temperature follows as usual to complete one time-step cycle.

Apart from this Durran-method we suggest still a *second method*. This approach attempts to avoid the introduction of the KDB-RUBC into the vertically implicit time-scheme, but it applies this boundary condition in an explicit way rather. We demonstrate this as follows. For that purpose we need not modify the uppermost gridpoint placement as necessary in the previous method and shown in Figure 13a, b. The gridpoint arrangement demonstrated in Figure 13a is maintained, and the only modification is to assume $\hat{w} \neq 0$ at the upper boundary (at $k^{'} = ke1$) owing to the RUBC:

$$\hat{w}_{top}^{(\tau+1,\tau)} = \frac{kc_s}{g\bar{\rho}_{top}\sqrt{\kappa-1}}\hat{p}_{top}^{(\tau+1,\tau)} \tag{84}$$

which is a rearranged form of the KDB-RUBC ((81) , (82)). Provided this vertical motion value is prescribed at the upper boundary, the prognostic step for pressure with (36) and for potential temperature (38) is possible for $k = ke$ with easy access to this boundary value. In order to execute the prognostic step for the vertical motion before by solving its tri-diagonal vertical structural equation set, the corresponding equation for $k^{'} = ke^{'}$ is slightly modified compared to the form in (43). Taking into account the significant boundary value, its contribution is added to the $ke^{'}$ - equation as follows

$$A_{ke'}\hat{w}_{ke'-1}^{(\tau+1)} + B_{ke'}\hat{w}_{ke'}^{(\tau+1)} = D_{ke'}^{(\tau)} - C_{ke'}\hat{w}_{top}^{(\tau)} \tag{85}$$

Here, the closure approximation is made to put the boundary value term on the right-hand side, where it is applied at the discrete time level τ instead of $\tau + 1$. From a practical point of view this small retardation is found to be irrelevant. In order to determine $\hat{w}_{top}$ from the KDB-RUBC (84), we need, however, the perturbation pressure $\hat{p}_{top}$ which is not directly available from the general time-stepping procedure. Thus, an extrapolation technique is invoked. The practical experimentation has shown that the application of some formal mathematical extrapolation is unsuitable. A successful method consists in using an adequate hydrostatic extrapolation. For that purpose it has shown to be necessary to use the consistent hydrostatic part of the prognostic $\hat{w}$ - equation with the given time-scheme included. In the present case we have to use the hydrostatic part of (26) which is here applied with L-grid and forward vertical differences:

$$\beta^{+}\frac{\hat{p}_{top}^{(\tau+1)} - \hat{p}_{ke}^{(\tau+1)}}{\Delta z/2} + \beta^{-}\frac{\hat{p}_{top}^{(\tau)} - \hat{p}_{ke}^{(\tau)}}{\Delta z/2} = -\frac{g}{c_s^2}\left(\beta^{+}\hat{p}_{ke}^{(\tau+1)} + \beta^{-}\hat{p}_{ke}^{(\tau)}\right) + \frac{g\bar{\rho}_{ke}}{\bar{\theta}_{ke}}\hat{\theta}_{ke}^{(\tau)} \tag{86}$$

This relation makes it possible to determine $\hat{p}_{top}^{(\tau)}$ as the input value in the KDB-RUBC (84) to determine $\hat{w}_{top}^{(\tau)}$, provided the prognostic step for the perturbation pressure with equation ((36), (37)) is made before.

This is our *second method* which is an explicit approach compared to the *first method* suggested from Durran (1999). The following application of both methods to our nonhydrostatic toy-model will be shown to be practically equivalent, though the Durran-approach demonstrates a perfect incorporation and adaptation to the given vertically implicit time-scheme, while our *second method* brings about some slight inaccuracies concerning the precise time-level assignment for $\hat{w}_{top}$ within the given time-scheme. Nevertheless, the latter approach promises to be a more simple method without troublesome preparatory changes in a given model and with more convenient properties for using different time-schemes. For numerical experimentation it becomes much more easy in the programming code to switch on/off the RUBC.

4.3 Results with KDB-RUBC

Here, we carry out toy-model simulations with KDB-RUBC instead of an upper lid-condition. We are going to apply both methods as explained in the previous Subsection, but the results shown in the following do not differ from each other at all. All the results up to now demonstrated with upper lid-condition have been repeated with KDB-RUBC involved and will be shown in the next Figures against the corresponding model version with upper lid. Figure 14 gives a comparison of lid-condition against RUBC for L- and CP-grid and in each panel for a horizontal wave component with 250km-wavelength.

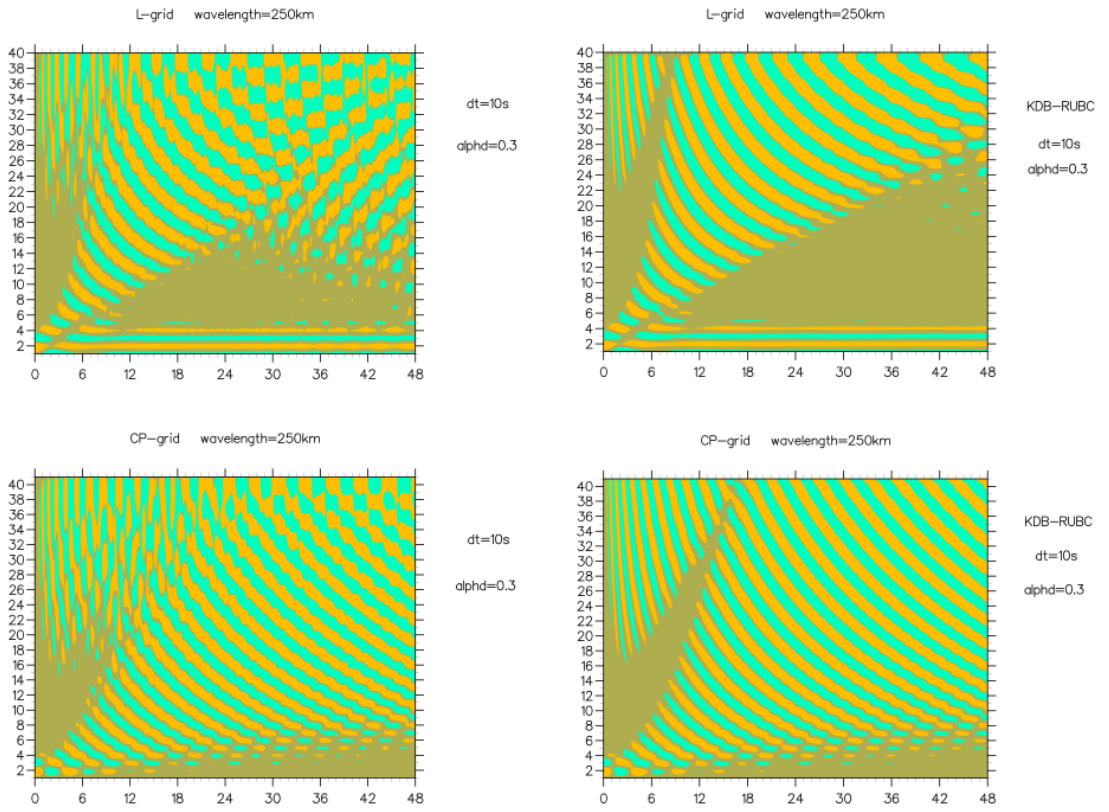

Figure 14: Simulations over 48 hours with 250km horizontal wavelength and both L- and CP-grid. Panels on the left row show the integrations with upper lid-condition, and the panels on the right row demonstrate the solution with KDB-RUBC involved.

The same type of simulation results follow immediately in Figure 15 for the potential temperature perturbation amplitude of a 100km horizontal wavelength.

In both figures (Figures 14, 15) the effect of the KDB-RUBC is clearly demonstrated. The reflective mode is essentially removed against the case with upper-lid condition. Thus, the advantages of the CP-grid on the one side and the disadvantages of the L-grid on the other side are much better revealed if a radiative upper boundary is assumed. In this case it is demonstrated best, how a dispersion process, here initiated by some special local imbalance of the hydrostatic basic state can be properly simulated. In spite of very specific and isolated simulations, deliberately adopted from Arakawa and Konor (1996) for methodical reasons, we still draw a more general conclusion that the L-grid can produce obvious shortcomings concerning the simulation of a possible dispersion process on the background of a given spectrum of internal gravity modes. Only in case of a CP-grid this dispersion process can be supported by a wide range of internal modes and is therefore simulated quite well, while using an L-grid, significant distortions of that process occur. In the latter case the associ-

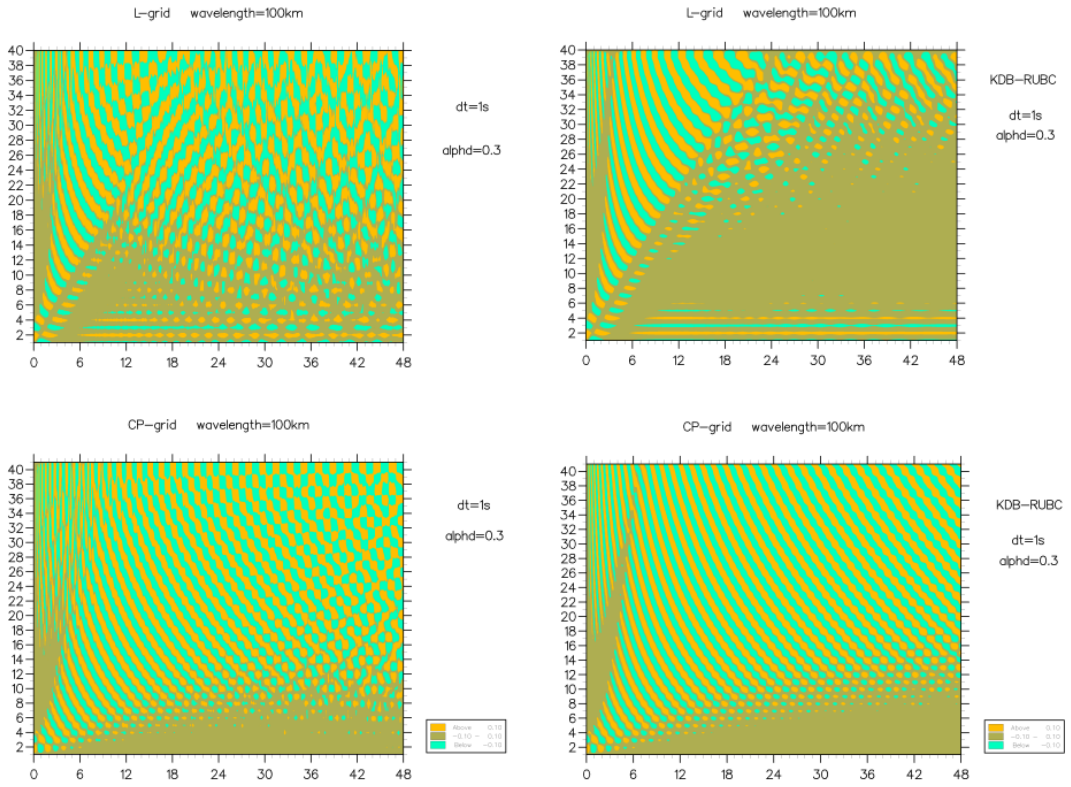

Figure 15: The same as in Figure 14 , but for 100km horizontal wavelength instead of 250km. Further explanation see text.

ated spectrum of internal modes is distorted, becomes shrunk, and brings about even an unphysical stationary mode.

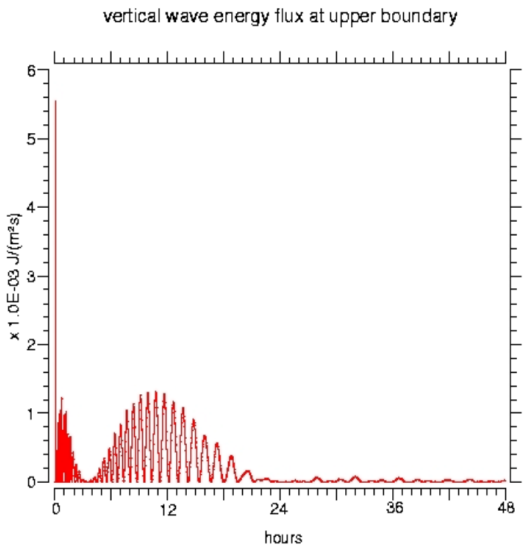

Figure 16: Vertical flux of wave energy over 48hour simulation with L-grid and 100km horizontal wavelength indicating how effective the KDB-RUBC operates

In Figure 16 we show the effectiveness of the KDB-RUBC for the L-grid simulation associated to the upper right panel of Figure 15. There can be seen the quantitative evaluation of the vertical flux of mechanical wave energy at the upper boundary in terms of $(\hat{p}\hat{w})_{top}$. This expression has to have a

positive sign in case of outgoing radiation, and Figure 16 demonstrates this positiveness over the 48 hour simulation time. The fastest vertically propagating signals associated to highest frequencies of the energy flux arrive at the upper boundary first, while after some gap the bulk of energy impinges on the model top at around 12 hour integration time having then the broadest amount of outgoing energy with slower frequencies. After that time increasingly less wave energy propagates upward, because most of it remains trapped as a stationary computational mode due to the L-grid properties, and, thus, the amount of outgoing energy dyes off over the following time.

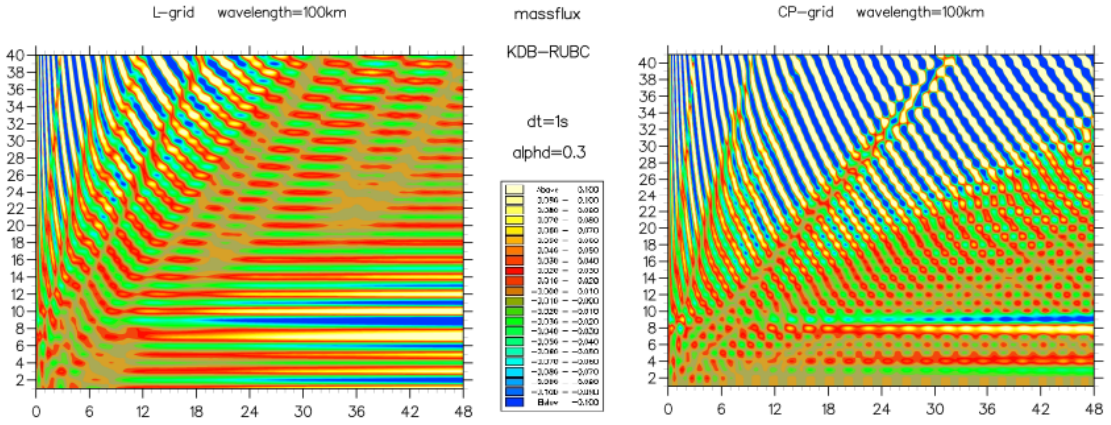

Figure 17: Time evolution of the potential temperature perturbation with imposed subgrid-scale massflux with L-grid versus CP-grid and with KDB-RUBC (compare with Fig.11).

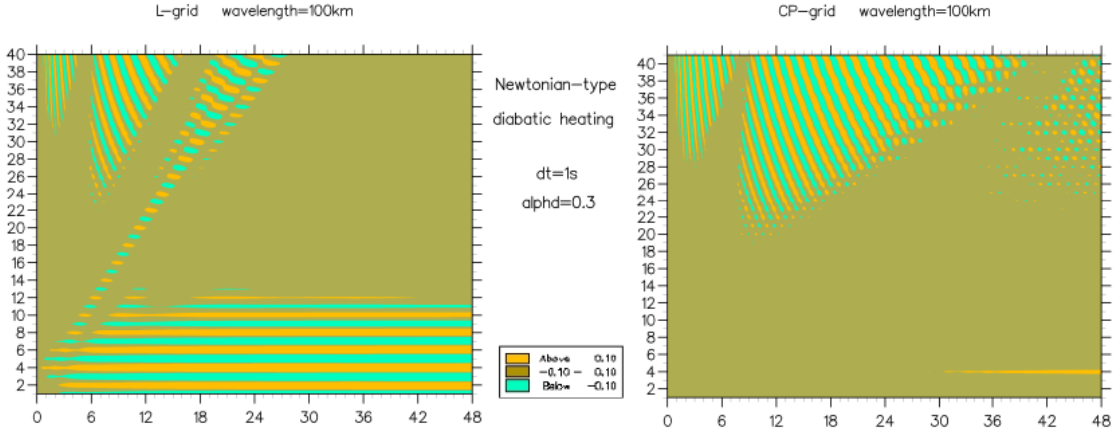

Figure 18: Simulation with Newtonian-type heat forcing at a single model level for horizontal wavelength of 100km and L-grid versus CP-grid, here with KDB-RUBC taken into account (compare with Fig.10).

Finally, we demonstrate the KDB-RUBC influence also from simulations already discussed in Subsection 3.7 for L-grid versus CP-grid, but executed there with upper lid-condition, where a simplified convective massflux and an Newtonian-heating case has been shown. A direct comparison without and with KDB-RUBC can be seen from Figure 10 versus Figure 18 in case of the Newtonian-heating simulation, and Figure 11 versus Figure 17 concerns the vertical massflux situation. The finding is also here that due to the impact of the KDB-RUBC the advantages of the CP-grid choice is much more distinct against the more distinct shortcomings of comparable L-grid simulations.

5 Simulations with LM - layering

All our previous simulations have used a vertical layering as proposed from Arakawa and Konor (1996). Instead of their choice of 40 geometrically equidistant vertical layers, we want to adopt now the vertically non-equidistant distribution of layers as valid in the LM. According to this a new experimental set-up with 35 layers is chosen from the COSMO LM-documentation by Doms and Schättler (2002, A description of the Nonhydrostatic Regional Model LM, Part I: Dynamics and Numerics, LM_F90 2.18, Nov.2002, at pages 57, 58 in Tables 4.1 and 4.2). In accordance with this the new vertically dicretised structure is formed by 35 main-levels and 36 half-levels, respectively. Since we remain here with a vertical z_k - coordinate as in the constant-layer model version above, the vertical z_k - distribution is adopted from the tables referred. For the present the basic state is assumed to be isothermal and not yet polytropic as normally used in the LM. On this basis the given LM fast-mode toy-model has been reformulated and extended to have then the LM - vertical layering. This has been made both for the vertical L-grid and the CP-grid staggering and in each case with KDB-RUBC omitted or involved. The documentation of all these modifications is rather lengthy and will therefore be dropped here.

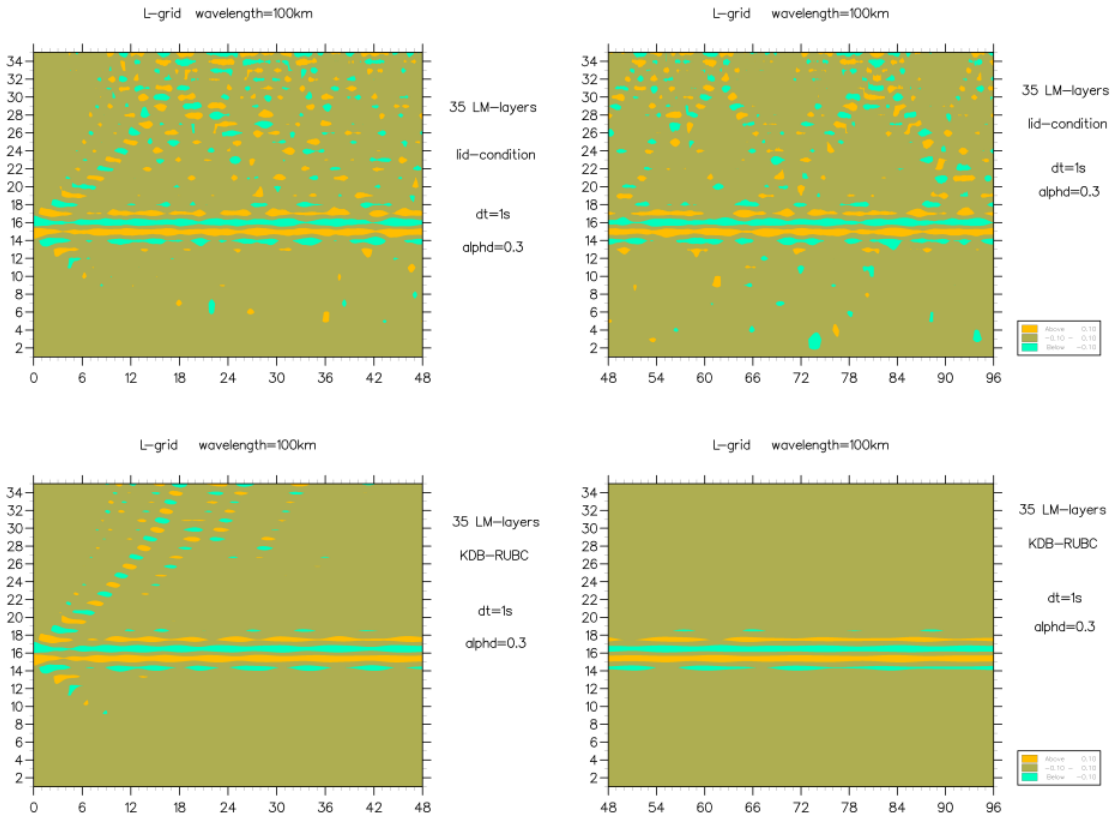

Figure 19: Time-height plot of potential temperature perturbation over 96-hour simulation time for L-grid with non-equidistant LM-layering , starting from an initial zig-zag perturbation. Upper row of panels: upper lid-condition. Lower row of panels: use of KDB-RUB. Each right panel is the continuation in time of the corresponding left one.

A simulation up to 96 hour integration time is shown in this context in Figure 19, where the typical L-grid deficiency can also be demonstrated and is more obvious with KDB-RUBC involved. The latter measure avoids a reflective mode downward from the upper boundary, so that almost all wave energy from the initial zig-zag perturbation with $\pm 0.5K$ prescribed only at vertical gridpoints $k = 15/16$ remains concentrated in an unphysical computational mode all over the integration time. It is interesting to note that the dispersion process triggered by the initial perturbation assumed here brings

about quite a different behaviour compared to all previous simulations with an equidistant layering adopted from Arakawa and Konor (1996). We postpone a deeper discussion of this numerical aspect beyond this report. Nevertheless, an anyhow triggered dispersion process with internal gravity modes involved depends for a given source strength on the thickness of layers and the way how the thickness of layers is varied through the depth of the model atmosphere (Gassmann 2003). In contrast to the L-grid simulation we show the comparable CP-grid case in the following Figure 20.

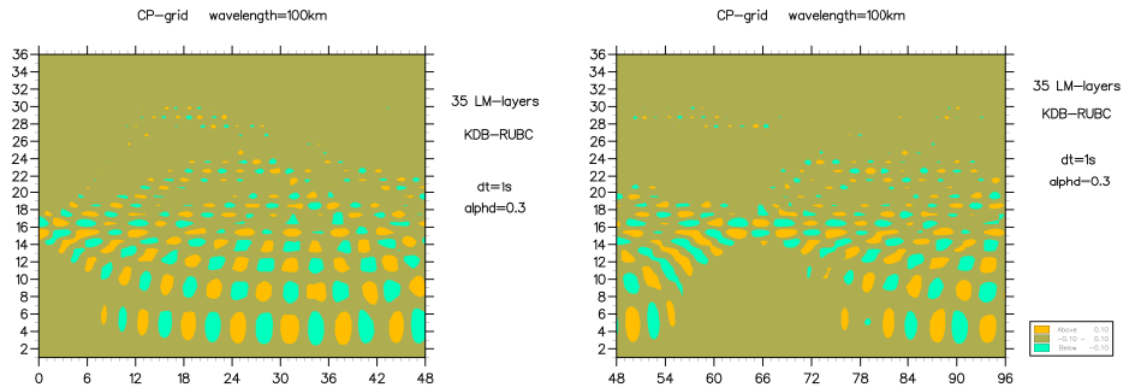

Figure 20: Comparable to Fig 19 the simulation with CP-grid property and KDB-RUBC involved.

We show here the simulation with KDB-RUBC only, since the related case with upper lid-condition has found to be not significantly different when using the CP-grid and having an initial zig-zag triggering at levels as assumed here. Compared to the result in Figure 19 it is demonstrated that the stationary computational mode is removed as expected, but the propagation of gravity modes behaves clearly different. Almost all wave energy seems trapped in the lower part of the model atmosphere where even reflections at the lower boundary can be observed. Although worth discussing these aspects we skip that here and restrict ourselves to the demonstration of L-grid shortcomings versus CP-grid advantages also in case of a vertical distribution of layer thickness used in the LM.

6 Conclusion

Starting point of our contribution was a paper by Arakawa and Konor (1996), in which these authors have carried out numerical simulations demonstrating important differences between the vertical grid type L and CP. They have shown that the L-grid version of their linear primitive model produces a computational mode without any physical meaning, while a model version with the CP-grid instead avoids this shortcoming. A thorough discussion including also quotations from many other authors are found in Arakawa (2000). We were particularly interested in the approach of Arakawa and Konor, because they have used a linearised hydrostatic model version as a simple and serious research tool, which is easy to copy for own investigations. After methodical studies with this model and with the identical experimental set-up we have then changed the model type to a compressible nonhydrostatic equation set in view of the linear fast-mode part of the LM. In order to be able to compare the solutions from this system with Arakawa and Konor's (1996) as close as possible, the design of vertical differencing (40 equally spaced layers), the choice of a basic state (isothermal and at rest) and the specific initialisation exactly remains as suggested by Arakawa and Konor. The model equations are written in spectral form for a horizontal wave component with vertically dependent perturbation amplitudes. The time-evolution of them can thus be investigated so as they are affected by the presence of gravity and sound wave modes. The given model design separates the combined effect of vertical differencing (layering, staggering) and LM - fast wave time-scheme with divergence damping involved in an isolated manner. First of all we apply this model tool in order to study computational influences on the dispersion process triggered by initially defined perturbations when using either the L-grid or the CP-grid. Within the scope of this investigation with a compressible nonhydrostatic model type very similar to the linearised LM fast mode equation part, we were also able to show that the CP-grid model version is clearly superior to an application of the L-grid in that model. Thus, there is a strong suspicion that the disadvantages of the L-grid demonstrated are expected to be possible also with the LM.

An important by-product of our simulations with L-grid versus CP-grid is that we have succeeded in incorporating the KDB-RUBC in the given scheme. The results without it suffer from strong reflections of gravity wave energy as a nuisance at and from the upper model-lid downward. Our investigation has shown that the application of the KDB-RUBC is possible and also successful in case of the nonhydrostatic compressible LM-like fast-mode model. Two methods how to incorporate the KDB-RUBC in this model has been tested. The first one is adopted from Durran (1999), and a second one is an explicit method. Both methods are equally successful showing almost identical results. In view of the present studies the impact of simulations with the KDB-RUBC included show that the advantage of a CP-grid is found to be much more distinct against the more distinct disadvantages with the L-grid.

Finally, we emphasise the meaning of our simple simulation model, that it is closely related to the linearised LM – fast mode equation part. In the sense of *res severa verum gaudium* it is a nice toy-model to study with it different options of time difference approximations in order to come then to an optimal time scheme for the LM as a whole. Furthermore, it is also possible to make studies concerning the proper way of layering through the vertical which seems also far from optimal.

Acknowledgement: The authors appreciate Peter Meyring's important help to convert the original text into the desirable LaTeX-form.

7 References

Arakawa, A. 2000: Future Development of General Circulation Models, in: General Circulation Model Development. Past, Present, and Future. Ed. By. Randall, International

Arakawa, A., and C.S. Konor, 1996: Vertical Differencing of the Primitive Equations Based on the Charney-Phillips Grid in Hybrid $\sigma - p$ Vertical Coordinates. Monthly Wea. Rev., 124, 511-528.

Bougeault, Ph., 1983: A nonreflective upper boundary condition for limited-height hydrostatic models. Monthly Wea. Rev., 111, 420-429.

Doms,G., and U. Schättler, 2002: A Description of the Nonhydrostatic Regional Model LM. Part I: Dynamics and Numerics. COSMO-Document, Nov. 2002, 134 pp.

Dudhia, J., 1993: A nonhydrostatic version of the Penn.State/ NCAR mesoscale model: Validation tests and simulation of an Atlantic cyclone and cold front. Monthly Wea. Rev., 121, 1493-1513.

Durran, D.R., 1999: Numerical methods for Wave Equations in Geophysical Fluid Dynamics. Springer-Verlag New York Berlin Heidelberg, 465 pp.

Gassmann, A., 2003: Formulation of the LM's Dynamical Lower Boundary Condition. COSMO Newsletter No.4, 155-158.

Gossard, E.E., and W.H. Hook, 1975: Waves in the Atmosphere. Elsevier Scientific Publishing Company Amsterdam-Oxford-New York, 456 pp

Ikawa, M., 1988: Comparison of some schemes for nonhydrostatic models with orography. J.Meteor.Soc.Jap., 66, 735-776.

Klemp, J.B., and D.R. Durran, 1983: An upper boundary condition permitting internal gravity wave Radiation in numerical mesoscale models. Monthly Wea. Rev., 111, 430-444.

Skamarock, W.C., and J.B. Klemp, 1992: The stability of time-split numerical methods for the hydrostatic and the nonhydrostatic elastic equations. Monthly Wea. Rev., 120, 2109-2127.

Author's adress:

Hans-Joachim Herzog,
DWD FE14, Potsdam
eMail: hans-joachim.herzog@dwd.de

Almut Gassmann,
Meteorological Institute, University Bonn
eMail: almut.gassmann@uni-bonn.de

List of COSMO Newsletters and Technical Reports

(available for download from the COSMO Website: www.cosmo-model.org)

COSMO Newsletters

Newsletter No.1, February 2001.

Newsletter No.2, February 2002.

Newsletter No.3, February 2003.

Newsletter No.4, February 2004.

COSMO Technical Reports

No. 1, Dmitrii Mironov and Matthias Raschendorfer (2001):
Evaluation of Empirical Parameters of the New LM Surface-Layer Parameterization Scheme. Results from Numerical Experiments Including the Soil Moisture Analysis.

No. 2, Reinhold Schrodin and Erdmann Heise (2001):
The Multi-Layer Version of the DWD Soil Model TERRA_LM.

No. 3, Günther Doms (2001):
A Scheme for Monotonic Numerical Diffusion in the LM.

No. 4, Hans-Joachim Herzog, Ursula Schubert, Gerd Vogel, Adelheid Fiedler and Roswitha Kirchner (2002):
LLM — the High-Resolving Nonhydrostatic Simulation Model in the DWD — Project LITFASS. Part I: Modelling Technique and Simulation Method.

No. 5, Jean-Marie Bettems (2002):
EUCOS Impact Study Using the Limited-Area Non-Hydrostatic NWP Model in Operational Use at MeteoSwiss.

No. 6, Heinz-Werner Bitzer and Jürgen Steppeler (2002):
Documentation of the Z-Coordinate Dynamical Core of LM.

No.7, Hans-Joachim Herzog, Almut Gassmann (2005):
Lorenz- and Charney-Phillips vertical grid experimentation using a compressible nonhydrostatic toy-model relevant to the fast-mode part of the 'Lokal-Modell'

COSMO Technical Reports

Issues of the COSMO Technical Reports series are published by the *Consortium for Small-Scale Modelling* at non-regular intervals. COSMO is a European group for numerical weather prediction with participating meteorological services from Germany (DWD, AWGeophys), Greece (HNMS), Italy (UGM, ARPA-SMR) and Switzerland (MeteoSwiss). The general goal is to develop, improve and maintain a non-hydrostatic limited area modelling system to be used for both operational and research applications by the members of COSMO. This system is initially based on the Lokal-Modell (LM) of DWD with its corresponding data assimilation system.

The Technical Reports are intended

- for scientific contributions and a documentation of research activities,
- to present and discuss results obtained from the model system,
- to present and discuss verification results and interpretation methods,
- for a documentation of technical changes to the model system,
- to give an overview of new components of the model system.

The purpose of these reports is to communicate results, changes and progress related to the LM model system relatively fast within the COSMO consortium, and also to inform other NWP groups on our current research activities. In this way the discussion on a specific topic can be stimulated at an early stage. In order to publish a report very soon after the completition of the manuscript, we have decided to omit a thorough reviewing procedure and only a rough check is done by the editors and a third reviewer. We apologize for typographical and other errors or inconsistencies which may still be present.

At present, the Technical Reports are available for download from the COSMO web site (www.cosmo-model.org). If required, the member meteorological centres can produce hardcopies by their own for distribution within their service. All members of the consortium will be informed about new issues by email.

For any comments and questions, please contact the editors:

Ulrich Schättler
ulrich.schaettler@dwd.de

Andrea Montani
amontani@smr.arpa.emr.it